HIRDLS - Straylight and Thermal background control requirements and Preliminary Estimates of background signals at the detectors

h

- Tony Richards -

Optics Group

h

Daresbury-Rutherford Appleton Laboratory
Chilton
Didcot
Oxfordshire OX11 0QX

h

This issue 1.1	22 April, 2013
Previous issues	
Issue 1.0	22 April, 1994

Contents

1.0 Introduction **3**

2.0 Major stray background sources of IR radiation **3**

3.0 HIRDLS Baseline optical system layout **5**

4.0 Telescope parameters and Detector sizes **5**

5.0 Filter bands, Expected atmospheric, background and radiometric noise radiances **6**

6.0 Expected signal sizes **6**

7.0 Estimating blackbody thermal emission signals **7**

8.0 Stray Solar and earth thermal radiation levels **8**

9.0 Mirror thermal emission signals **9**
- **9.1 Primary mirror emission onto the detector** **10**
- **9.2 Scan mirror emission onto the detector** **11**

10.0 Earth + structure thermal emission scattered from mirrors **12**
- **10.1 An important assumption** **13**
- **10.2 Typical mirror-scatter performance calculations** **14**
- **10.3 Primary mirror viewing geometry** **16**
- **10.4 Scan-mirror viewing geometry** **16**

11.0 Variation in the mirror-scattered radiances due to viewing geometry variations **17**
- **11.1 Simplified geometry for order-of-magnitude calculations of scattered-signal variations** **17**

12.0 Estimating Diffraction effects **19**
- **12.1 The Airy diffraction formula** **19**
- **12.2 The Bi-directional Diffraction Distribution Function (BDDF)** **21**
- **12.3 Diffractive scatter estimates using the Airy BDDF** **22**
- **12.4 Additional complications to diffraction estimates** **23**

13.0 Comparison of expected scatter radiances and background budget values **27**
- **13.1 Background Budgets** **27**
- **13.2 Diffractive scatter compared with budgets** **28**
- **13.3 Incoherent (surface) scatter compared with budgets** **29**

14.0 Conclusions from the Comparison of diffractive and incoherent scatter with budgets **30**

Appendix A: Tables 8, 9 and 11 ..... **32**
- **Tables 8A - 8I Surface scatter fractions** **33**
- **Tables 9A-9F Surface scatter fractions** **36**
- **Table 11 Diffractive scatter estimates** **38**

Appendix B : 21- channel Atmospheric radiance curves, figures B1 - B21 ..... **41**

HIRDLS - Straylight and Thermal background control requirements and Estimates of background signals at the detectors

1.0 Introduction

The HIRDLS instrument is an earth's atmosphere observing instrument, intended to map the concentrations of various chemical species over a range of heights in the earth's atmosphere by imaging a grid of areas of atmosphere near the earth's limb onto a grid of infra-red sensitive, cooled detectors . Coverage of a range of instrument lines-of-sight (LOS) positioned from a few to ≅ 100 km above the earth's limb will be achieved by the combination of the spatial spread of the detector grid in the height direction combined with an ability to scan the grid in the height direction (the altitude scan). Coverage of the whole of the earth's atmosphere will be achieved by observing continuously from a sun-synchronous low earth orbit (LOE) combined with the ability to scan the view presented to the detector grid in a plane at 90 degrees to the altitude scan direction (the azimuth scan).

HIRDLS is intended to have high sensitivity and high radiometric accuracy but it is intended to achieve both without the necessity to cool the telescope optics. It is intended to calibrate out or subtract fairly large thermal offsets by a combination of mechanical chopping and phase-sensitive detection of the atmospheric signal (removing any constant background signal originating from the space between the chopper and the detectors) and by scanning the instrument view to 'space' (when any remaining 'constant' background component originating within the space in front of the chopper will be determined). This scheme presupposes a stable temperature environment for the most important instrument surfaces (those viewed by the detector and those illuminating structure viewed by the detectors).

Stringent budgets have been allotted to various sources of signal measurement errors and it is the task of the straylight analysis to determine if the HIRDLS instrument design will be capable of restricting the stray background component of the radiation reaching the detectors to values specified by the budgets.

Since HIRDLS is an IR sensitive instrument, there will be a background component of thermal origin contributed by elements of the optical system which the detectors see directly (or via specular reflections from mirror surfaces). This 'in field-of view' (IFOV) component has been given its own budget for contributing to signal measurement error. A separate budget has been allotted to the 'out of field-of-view' (OFOV) components. Further discussion of background budgets and their comparison with estimates of scatter radiances can be found in sections 13 and 14.

The main conclusion of this preliminary study is that diffraction of near-FOV earth radiance will dominate over mirror-surface scatter and to exceed background budgets substantially (up to a factor x75), necessitating the addition to the HIRDLS design of some method of substantially reducing the diffractive contribution to the background.

2.0 Major stray background sources of IR radiation

The major sources of infra-red radiation likely to be troublesome to the HIRDLS instrument are

*solar radiation (6000K blackbody) shining directly into the instrument
*solar radiation scattered from the Earth into the instrument (specularly and diffusely reflected 6000K blackbody radiation)
* solar radiation scattered by external spacecraft surfaces into the instrument

* Thermal emission from the Earth into the instrument directly onto the optics and then scattered or diffracted to the detectors (chopped and unchopped)
* Thermal emission from internal spacecraft structure directly to the detectors (chopped and unchopped)
* Thermal emission from internal spacecraft structure to the detectors via specular reflections from the optics (chopped and unchopped)
* Thermal emission from internal spacecraft structure to the detectors via non-specular scatter from the optics (chopped and unchopped)

Before a detailed analysis of the HIRDLS instrument is carried out it is instructive to make reasonably accurate estimates of the magnitudes of the likely sources of interfering radiation and to order them into decreasing order of size as a way of classifying their importance when considering the development of a HIRDLS straylight control philosophy and as an aid to

identifying design-drivers. This will be done in the subsequent sections after the baseline HIRDLS optical system is presented. (The order in which the straylight sources are presented is not necessarily the order given in the above list)

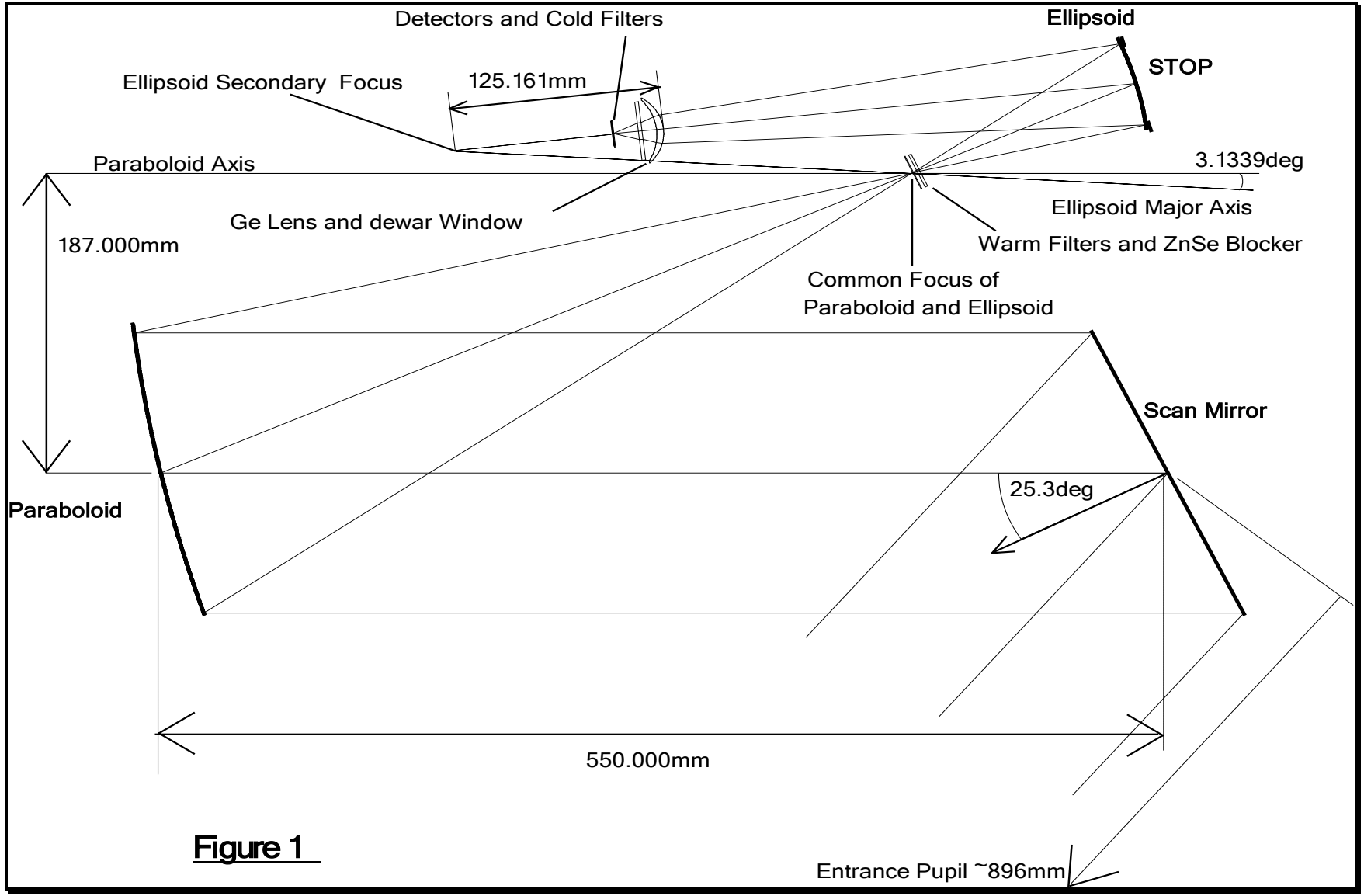
Detectors and Cold Filters
Ellipsoid
STOP
Ellipsoid Secondary Focus
125.161mm
Paraboloid Axis
3.1339deg
Ellipsoid Major Axis
Ge Lens and dewar Window
187.000mm
Warm Filters and ZnSe Blocker
Common Focus of
Paraboloid and Ellipsoid
Scan Mirror
25.3deg
Paraboloid
550.000mm
Entrance Pupil ~896mm

Figure 1

3.0 HIRDLS Baseline optical system layout

Figure 1 shows a baseline design for the HIRDLS optical system. There are 21 detector channels located behind a set of narrow band filters and at the focus of a Germanium lens. The detectors are arranged in 3 evenly-spaced columns of seven each. The Ge lens forms virtual images of the detectors near one focus of the ellipsoid and the ellipsoid images these near its second focus, the latter being coincident with the prime focus of the paraboloidal primary mirror. Thus the detectors are imaged by the lens and ellipsoid to plane at the focus of the primary mirror. Since the aperture stop is not at the primary mirror, the latter will be slightly oversized.

From the straylight point of view, we can consider that the detectors 'exist' at the prime focus of the paraboloid, so that any light which reaches an image of a detector at this point and which falls within the cone of rays converging from the primary mirror will be transferred by the subsequent optical system (ellipsoid + lens) to the physical detectors.

Just in front of the prime focus is located a field-stop mask and a set of broad-band filters matched to each detector. Also in this vicinity will be located a mechanical chopper to modulate the atmospheric signal (and any superimposed background) to permit phase-sensitive detection against a possibly large unchopped background. A scan mirror, nominally tilted at 25.3 degrees to the optical axis, is also slightly oversized and is used to put different parts of the earth's atmosphere onto each detector by rotations about two orthogonal axes (the altitude and azimuthal scan axes).

In the following, reference to 'detectors' at the prime focus must be taken to mean the apertures in the field stop located there and which are matched to the image of each detector formed there by the subsequent ellipsoid mirror and the lens.

It is clear from the design that all optics and surfaces in the space viewed by the physical detectors (between them and the chopper) should fall within or form the walls of a sealed volume whose only source of radiation input from 'outside' must be the aperture mask in front of the chopper. Many of these surfaces (including the back of the chopper) can contribute direct thermal radiation to the detectors ('direct' includes mirror-reflections and lens refractions). The rest can contribute thermal radiation by scattering from optical surfaces. It remains to see what are the consequences of not cooling most of this structure.

4.0 Telescope parameters and Detector sizes

Each physical detector is masked to expose a 0.082 mm X 0.82 mm rectangle at the final focal plane. Therefore the physical detector area $A_{ph} = 6.72\text{x}10^{-8}$ m^{2}. The telescope's effective focal length (EFL) is 247 mm, giving a projected solid angular size $\Delta\Omega_d$ for each detector onto the sky of 68.5 x 685 arc-sec^2 ($1.1\text{x}10^{-6}$ steradian). The primary mirror's focal length, $\mathbf{F_p}$, measured from its pole is 0.455 metre. The cone of rays onto each detector from the primary mirror is about f/2.6 giving a half-cone angle $\mathbf{\Theta_p}$= 11 degrees approximately. The effective telescope aperture diameter D_{tel} =0.165 metre, giving an effective telescope aperture area, A_{tel}= 0.02138 m^2. The primary mirror is oversized slightly to a diameter ≅ 0.17 metre (as is the scan mirror). This physical data is summarised below.

Physical detector area ,	$\mathbf{A_{ph} = 6.72\text{x}10^{-8}\ m^2}$	(1.1)
Detector solid angular size on sky,	$\mathbf{\Delta\Omega_d = 1.1\text{x}10^{-6}}$ **steradian**	(1.2)
Effective telescope aperture diameter	$\mathbf{D_{tel}}$ **=0.165 metre**	(1.3)
Effective telescope aperture area,	$\mathbf{A_{tel}= 0.02138\ m^2.}$	(1.4)
Primary mirror focal length,	$\mathbf{F_p}$ **= 0.455 metre**.	(1.5)
Primary mirror diameter,	$\mathbf{D_p \cong 0.17}$ **metre**.	(1.6)
Primary beam f-number,	**f#** ≅ **f/2.6**	(1.7)
Primary beam half-cone angle,	$\mathbf{\Theta_p \cong 11}$ **deg**.	(1.8)

Since the scan-mirror and the primary mirror provide no angular magnification when projecting the sky onto the 'detectors' at the prime focus, the angular size of each of the detector images at the prime focus equals the angular size of the physical detectors on the sky. The physical size of the detector images at the prime focus is the detector physical size scaled up by the ratio F_p/EFL =455/247=1.842. This gives a detector image size of 1.842 x 0.082 mm by 1.842 x 0.82 mm = 0.15 mm x1.5 mm. Thus the effective area of a detector at the prime focus $A_d = 2.25 \times 10^{-7}$ m^2 .

Imaged Detector area at prime focus, $\mathbf{A_d = 2.25 \times 10^{-7}\ m^2}$ (1.9)

5.0 Filter bands, Expected atmospheric, background and radiometric noise radiances

Table 1 shows data taken from table 2 in the HIRDLS Instrument Requirements Document (IRD). It shows the combined filter pass-bands for each of the 21 detectors, R_α the maximum expected atmospheric radiances (watt/m^2/sr) in each channel and NEN_α, the expected radiometric noise radiances in each channel (N.B. in 10^{-4} watt/m^2/sr). The latter numbers are guides to the measurement noise expected in each channel and indicate the size of the smallest atmospheric radiance in each channel that the instrument should be capable of detecting and measuring accurately. (This signal will occur at different ILOS heights above the earth's limb in different channels). Column 6 ratios R_α and NEN_α , showing that the former exceeds the latter by a factor between 1400 and 34000, depending on the channel.

Column 7 shows typical radiances B_α (see section 7.0) expected from a 300K blackbody within each of the 50% pass bands. These values are a guide to expected thermal radiance from the earth's disk inside the limb and from internal spacecraft structure (e.g. the primary and scan mirrors) if this is not cryogenically cooled. This assumes that by thermal design the spacecraft structure will stabilise in flight at or near room temperature (taken as 300K). Column 8 ratios R_α and B_α and shows that only in the minority of channels does R_α exceed B_α . Taken with column 6 , it can be noted that B_α therefore exceeds NEN_α by even larger factors than R_α does in the majority of channels.

Table 1 HIRDLS spectral channels (from the Instrument Requirements Document)

Detector channel	species	50% pass band wavelengths λ_{min},λ_{max} (μ)	**R_α** Max Expected in-band Atmos. Radiance (watt/m2/sr)	**NEN_α** In-band Radio-metric Noise Radiance (10-4 watt/m2/sr)	**R_α/NEN_α**	**$B_\alpha(300)$** 300K Blackbody in-band radiance (watt/m2/sr)	**$R_\alpha/B_\alpha(300)$**
1	N2O,aerosol	17.01 - 17.76	2.21	12.0	1842	3.76	0.59
2	CO2	16.26 - 16.67	0.89	6.3	1413	2.49	0.36
3	CO2	15.63 - 16.39	1.62	5.9	2746	4.63	0.35
4	CO2	15.15 - 15.97	1.88	6.0	3133	4.99	0.38
5	CO2	14.71 - 15.27	1.56	4.3	3628	3.77	0.41
6	aerosol	11.96 - 12.18	2.55	1.9	13421	1.95	1.31
7	CClF3	11.72 - 11.98	3.06	2.0	15300	2.37	1.29
8	HNO3	11.05 - 11.63	7.19	2.1	34238	5.42	1.33
9	CCl2F2	10.72 - 10.93	2.51	2.0	12550	2.01	1.25
10	O3	9.95 - 10.15	1.48	1.5	9867	1.97	0.75
11	O3	9.35 - 9.80	1.48	2.4	6167	4.47	0.33
12	O3	8.77 - 8.93	1.21	1.0	12100	1.57	0.77
13	aerosol	8.20 - 8.33	0.89	1.1	8091	1.22	0.73
14	N2O5	7.94 - 8.14	0.78	1.1	7091	1.83	0.43
15	N2O	7.80 - 7.96	0.32	1.1	2909	1.38	0.23
16	ClONO2	7.70 - 7.82	0.19	1.1	1727	1.04	0.18
17	CH4	7.30 - 7.55	0.46	1.2	3833	2.12	0.22
18	H2O	6.97 - 7.22	0.43	1.2	3583	1.87	0.23
19	aerosol	7.06 - 7.13	0.15	1.3	1154	0.52	0.29
20	H2O	6.49 - 7.03	0.58	1.6	3625	3.85	0.15
21	NO2	6.12 - 6.32	0.16	1.1	1455	1.12	0.1

6.0 Expected signal sizes

Given the expected atmospheric radiances in table 1, we can compute the expected signals in watts at a detector located at the prime focus . If R_α is the atmospheric radiance in band α, the signal S_α in watts will be given by

$$S_\alpha = r_{sm} r_P R_\alpha \Delta\Omega_d A_{Tel} \qquad (2)$$

In the above, r_{sm} and r_P are scan- and primary mirror reflectivities. Taking 0.95 for each of these, we get

$$S_\alpha = 2.12 \times 10^{-8} R_\alpha \text{ watt} \qquad (3)$$

Table 2 gives S_α computed for each band using the maximum atmospheric R_α values given in table 1. Also given are the signals expected from the minimum radiances expected to be detectable. These are derived by dividing the maximum expected signals by the factors given in column 6 in table 1. These factors are repeated in column 5

Table 2 Maximum and Minimum Expected In-band Signal Sizes

Detector Channel	R_α Max. Expected in-band Radiance (watt/m2/sr)	S_α^{max} Max. Expected in-band signal (10-8 watt)	S_α^{min} Min. Expected in-band signal (10-12 watt)	$S_\alpha^{max}/S_\alpha^{min}$
1	2.21	4.69	25.5	1842
2	0.89	1.89	13.4	1413
3	1.62	3.44	12.5	2746
4	1.88	3.99	12.7	3133
5	1.56	3.31	9.1	3628
6	2.55	5.41	4.0	13421
7	3.06	6.49	4.2	15300
8	7.19	15.26	4.5	34238
9	2.51	5.33	4.2	12550
10	1.48	3.14	3.2	9867
11	1.48	3.14	5.1	6167
12	1.21	2.57	2.1	12100
13	0.89	1.89	2.3	8091
14	0.78	1.66	2.3	7091
15	0.32	0.68	2.3	2909
16	0.19	0.40	2.3	1727
17	0.46	0.98	2.6	3833
18	0.43	0.91	2.5	3583
19	0.15	0.32	2.8	1154
20	0.58	1.23	3.4	3625
21	0.16	0.34	2.3	1455

7.0 Estimating blackbody thermal emission signals

Thermal emission signal calculations require transmission factors for each of the detector pass-bands taking blackbody spectra for the signal sources. These factors depend on the location and width of the band and the temperature of each blackbody**.** If we denote these factors or fractions by $F_\alpha(T;\lambda min,\lambda max)$ where α=1-21 to identify one of 21 bands, then

$$F_\alpha(T;\lambda_{\min},\lambda_{\max}) = \int_{\lambda_{\min}}^{\lambda_{\max}} \frac{B(\lambda,T)d\lambda}{B(T)} \qquad (4)$$

This equation assumes 'top hat' filter transmission and detector response functions (i.e. unity within the band and zero outside it). B(λ,T) is the Planck function at temperature T. The source radiance B(T) (B(λ,T) integrated over all λ) is given by (with **σ=** Stefan's constant =5.67x10^{-8} watts/metre^2/° K^4 and **ε** the emissivity of the surface - the latter being assumed independent of λ)

$$B(T) = \varepsilon\sigma T^4 / \pi \text{ watts/metre}^2\text{/steradian} \qquad (5)$$

Note the dimensions chosen for B(T). The in-band radiances are then computed using

$$B_\alpha(T) = B(T)F_\alpha(T;\lambda min,\lambda max) \quad (6)$$

Table 3 gives $F_\alpha(T;\lambda_{min},\lambda_{max})$ and $B_\alpha(T)$ for the 21 filter bands considered for HIRDLS (using the 50% pass band values for λ_{min}, λ_{max}) for T = 6000K (sun) and T = 300K (earth and spacecraft internal surfaces). The $B_\alpha(T)$ values were computed assuming emissivity $\varepsilon = 1$. The maximum expected in-band atmospheric radiances are repeated from table 2 for comparison. Note that, except for channels 20 and 21, B_α and R_α values for T = 300K are within a factor 3 or 4 of each other. For T = 6000K, the B_α values exceed the R_α values by factors from 155 to 34000.

Table 3 T = 6000K and T = 300K Blackbody fractions and radiances for the 21 HIRDLS bands

Detector Channel	$F_\alpha(6000)$	$B_\alpha(6000)$ (watt/m2/sr)	F_α (300)	$B_\alpha(300)$ (watt/m2/sr)	R_α, Max. in-band Radiance (watt/m2/sr)	**B_α/R_α (6000K)**	**B_α/R_α (300K)**	**B_α/NEN_α (6000K)**	**B_α/NEN_α (300K)**
1	1.63x10-3	380.9	0.0257	3.76	2.21	172	1.7	316824	3131
2	1.75x10-3	409.1	0.0171	2.49	0.89	460	2.8	649980	3956
3	2.28x10-3	533.3	0.0317	4.63	1.62	329	2.9	903434	7963
4	2.46x10-3	575.4	0.0342	4.99	1.88	306	2.7	958698	8459
5	2.20x10-3	515.0	0.0258	3.77	1.56	330	2.4	1197240	8707
6	1.72x10-3	401.4	0.0133	1.95	2.55	157	0.8	2107097	10737
7	2.03x10-3	474.3	0.0162	2.37	3.06	155	0.8	2371500	12240
8	8.35x10-3	1953.0	0.0370	5.42	7.19	272	0.8	9312736	27390
9	3.02x10-3	707.3	0.0137	2.01	2.51	282	0.8	3539100	10040
10	3.51x10-3	820.9	0.0135	1.97	1.48	555	1.3	5476185	12827
11	1.22x10-2	2842.0	0.0306	4.47	1.48	1920	3.0	11840640	18501
12	4.32x10-3	1010.0	0.0107	1.57	1.21	835	1.3	10103500	15730
13	7.64x10-3	1788.0	0.0083	1.22	0.89	2009	1.4	16254819	11327
14	1.18x10-2	2751.0	0.0125	1.83	0.78	3527	2.3	25009957	16309
15	9.41x10-3	2200.0	0.0094	1.38	0.32	6875	4.3	19999375	12509
16	7.06x10-3	1650.0	0.0071	1.04	0.19	8684	5.5	14997268	9499
17	1.47x10-2	3438.0	0.0145	2.12	0.46	7474	4.6	28647842	17632
18	1.47x10-2	3438.0	0.0128	1.87	0.43	7995	4.3	28646085	15407
19	4.12x10-3	962.7	0.0036	0.52	0.15	6418	3.5	7406372	4039
20	4.19x10-2	9806.0	0.0264	3.85	0.58	16907	6.6	61287875	23925
21	2.33x10-2	5445.0	0.0077	1.12	0.16	34031	7.0	49515105	10185

8.0 Stray Solar and earth thermal radiation levels

From the straylight point of view, the most stringent requirement is going to be driven by the ratios given in columns 9 and 10 of table 3, where radiances typical of NEN values are compared to the sun and earth/structure blackbody radiances. **The numbers show that in order to ensure that the solar component is reduced to below NEN levels, the instrument must attenuate radiation of solar origin by a factor $\cong 10^8$. Similarly, to reduce the earth /structure component to below NEN levels will require an attenuation factor $\cong 10^5$**.

Scattering of solar radiation by the earth is estimated as follows. Figure 2 shows the geometry.

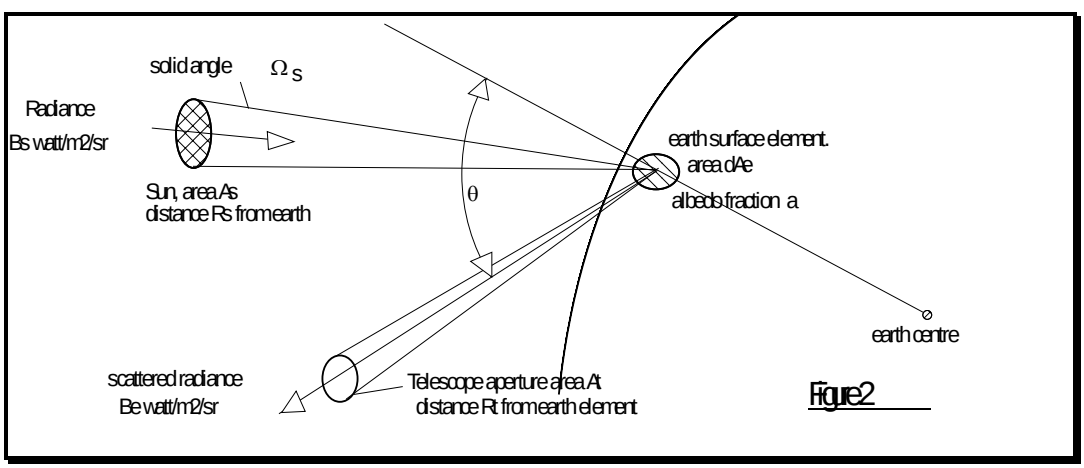

Figure2

If we assume diffuse scatter of a fraction **a** (the albedo) of the incident sunlight towards the aperture of an orbiting telescope, B_e , the effective radiance of the earth due to scattered sunlight as viewed by the telescope is given by

$$B_e = B_s \Omega_s a / \pi \quad (7)$$

Other symbols are defined in fig 2. B_e and B_s are in watts/m^2/sr. Table 4 shows B_e values computed using eq (7) with Ω_s = 6.8x10$^{\wedge -5}$ sr and using the sun's B_α values given in table 3. Column 3 gives B_e assuming a=1.0 and column 4 shows B_e assuming a=0.3 (a typical value for the visible part of the spectrum). They can be compared to the earth's B_α values taken from table 3. Table 4 shows that in the HIRDLS IR bands, signals due to sunlight scattered from the earth will be below the earth self-emission signal, provided that the sunlight is not specularly scattered towards the HIRDLS telescope.

Table 4 Estimated Radiances due to solar radiation scattered from the earth

Detector Channel	Sun B_α(6000) watt/m2/sr)	B_e albedo =1.0 (watt/m2/sr)	B_e albedo =0.3 (watt/m2/sr)	Earth B_α(300) (watt/m2/sr)
1	380.9	0.0083	0.0025	3.76
2	409.1	0.0090	0.0027	2.49
3	533.3	0.0117	0.0035	4.63
4	575.4	0.0126	0.0038	4.99
5	515.0	0.0113	0.0034	3.77
6	401.4	0.0088	0.0026	1.95
7	474.3	0.0104	0.0031	2.37
8	1953.0	0.0428	0.0128	5.42
9	707.3	0.0155	0.0046	2.01
10	820.9	0.0180	0.0054	1.97
11	2842.0	0.0622	0.0187	4.47
12	1010.0	0.0221	0.0066	1.57
13	1788.0	0.0391	0.0117	1.22
14	2751.0	0.0602	0.0181	1.83
15	2200.0	0.0482	0.0144	1.38
16	1650.0	0.0361	0.0108	1.04
17	3438.0	0.0753	0.0226	2.12
18	3438.0	0.0753	0.0226	1.87
19	962.7	0.0211	0.0063	0.52
20	9806.0	0.2147	0.0644	3.85
21	5445.0	0.1192	0.0358	1.12

9.0 Mirror thermal emission signals

Since the HIRDLS baseline design assumes uncooled mirrors, there may be significant thermal emission onto the detectors from those mirrors which are within the detectors' fields of view e.g. from the primary and scan-mirrors. In this section an estimate is made of the contributions expected from these sources. Figure 3 shows a general geometry used for evaluating thermal radiation arriving onto a flat detector from surfaces within a 2π solid angle forward of it.

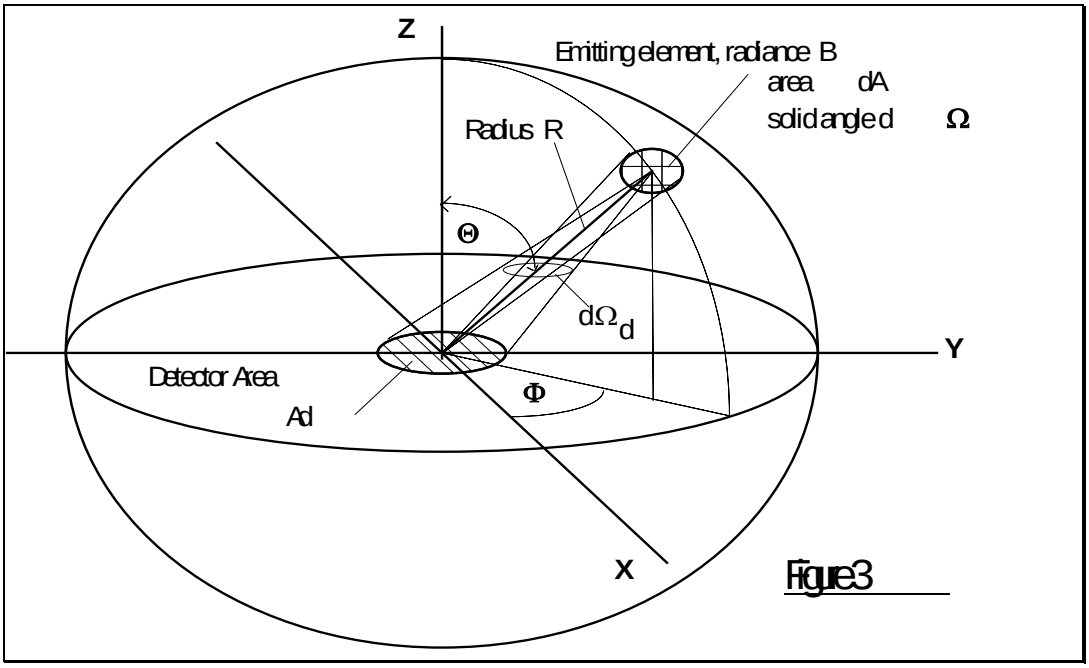

Let an emitting element, area **dA,** be located at (Θ,Φ) relative to the centre of a detector, area $\mathbf{A_d}$. The emitting element is a small part of a sphere, radius **R,** centred on the detector (see figure 3). This sphere is intended to represent a 'detector surround' which can be a real physical item or which may stand in for some or all of the surfaces which the detector can 'see' within a solid angle of 2π steradians centred on the normal to the detector. The following calculation estimates the likely thermal flux which will fall on the detector from an **isothermal** surround at temperature T °K.

The solid angle subtended by the detector when viewed from the emitting element is $\mathbf{d\Omega_d}$, where

$$d\Omega_d = A_d \cos\Theta / R^2 \qquad (8)$$

The solid angle **dΩ** subtended by the emitting element at the detector is given by

$$d\Omega = \sin\Theta d\Theta d\Phi \qquad (9)$$

The in-band radiance $\mathbf{B_\alpha}$ of the emitting element is in watts/m^2/steradian. The increment dE_α to the in-band flux falling onto the detector from an emitting element area dA is given by

$$dE_\alpha = B_\alpha \left[\frac{A_d}{R^2} \cos\Theta \right] dA \qquad (10)$$

The integrated flux falling from emitting elements in the angular ranges $\mathbf{\Theta_{min} \le \Theta \le \Theta_{max}}$ and $\mathbf{0 \le \Phi \le 2\pi}$ is given by

$$E_\alpha = \int_{\Theta,\Phi} B_\alpha \left[\frac{A_d}{R^2} \cos\Theta \right] dA \qquad (11)$$

By using the fact that $\mathbf{dA = R^2 d\Omega}$ and eq. **(9)** for **dΩ,** eq. **(11)** becomes

$$E_\alpha = \int_{\Theta_{min}}^{\Theta_{max}} \int_0^{2\pi} B_\alpha A_d \sin\Theta \cos\Theta d\Theta d\Phi = \pi B A_d \left[\frac{\cos 2\Theta_{min} - \cos 2\Theta_{max}}{2} \right] \mathbf{watts} \qquad (12)$$

If Θ_{min}=0 and Θ_{max}=90, then **E** reaches its maximum value $\mathbf{E_\alpha = \pi B_\alpha A_d}$**.** For small Θ_{min}, this approximation is good. Note that E_α is independent of the radius of the spherical surface making up the emitting surface**.** E_α only depends on the area of the detector, the radiance of the emitting surface and the solid angle that the emitter occupies in the field of view of the detector. Emission from the primary and scan mirrors will be estimated using the above.

9.1 Primary mirror emission onto the detector

Figure 4 shows the essential geometry. The ray-cone onto the detector at the prime focus has a half-angle Θ_P= 11 deg. Put Θ_{min}=0.0 and Θ_{max} = 11 deg in eq. (12) and use eq. (1.9) for A_d to get (with ε_P, T_P = primary emissivity and temperature)

$$E_\alpha^P = 2.57 \times 10^{-8}\, \varepsilon_P\, (B_\alpha(T_P)/\varepsilon) \text{watts} \quad (13)$$

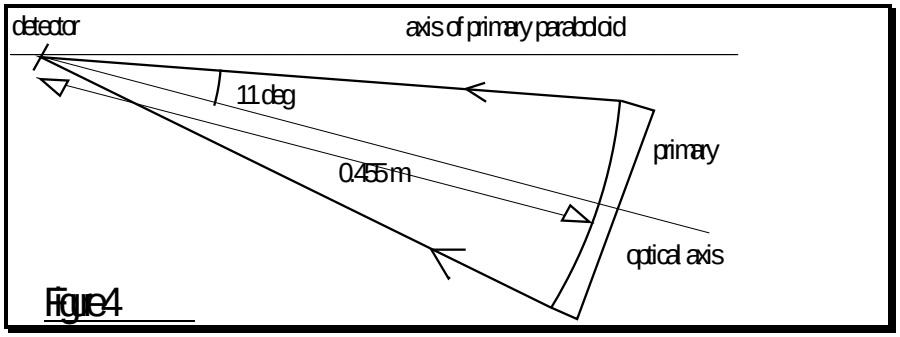

9.2 Scan mirror emission onto the detector

Figure 5 shows the essential geometry in this case. The angular size of the image of the prime focus 'detector' when viewed from the scan mirror through the primary mirror is the same as the angular size of the atmospheric element it samples, so we use eq. (10) with dA = the effective scan-mirror area (taken as nominally equal to the primary area, see eq.(1.6)) and with $A_d/R^2=\Delta\Omega_d$, the effective detector angular size on the sky (from eq. (1.2)). The result is (with ε_{SM}, T_{SM} = scan-mirror emissivity and temperature)

$$E_\alpha^{SM} = 2.5 \times 10^{-8}\, r_P\, \varepsilon_{SM}\, (B_\alpha(T_{SM})/\varepsilon) \text{watts} \quad (14)$$

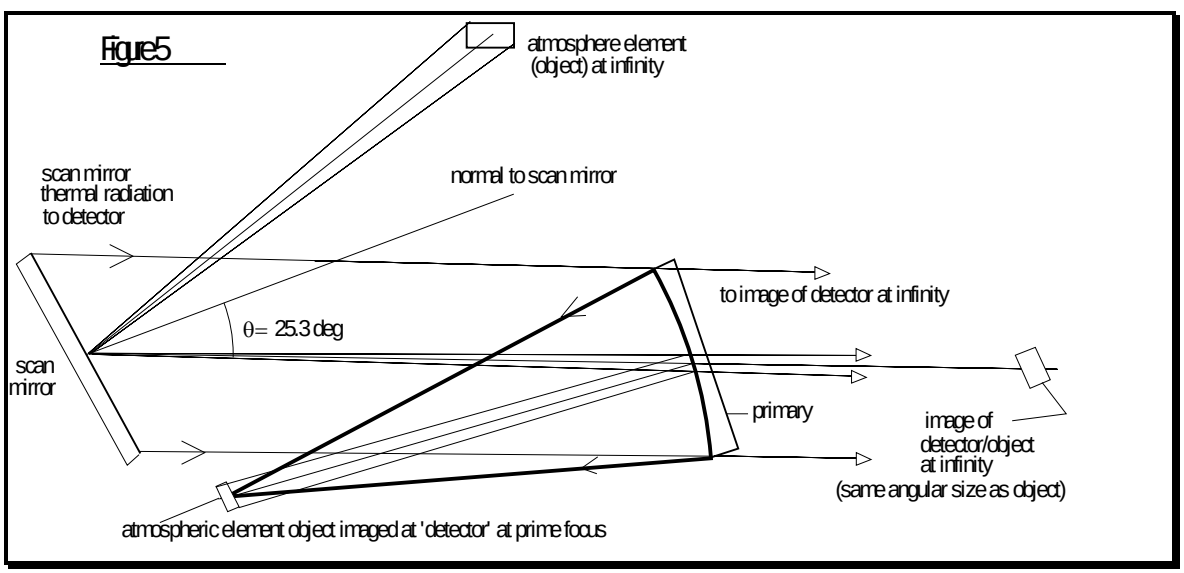

Note that the contributions from both mirrors (eqs (13) and (14)) are almost exactly equal if $r_p \cong 1$ and $\varepsilon_{SM} \cong \varepsilon_P$ and their temperatures are equal (these conditions are quite reasonable). Taking r_p=0.95 and $\varepsilon_{SM}=\varepsilon_P$=0.05 we find the values for $E^{TOT}_\alpha = (E^{SM}_\alpha + E^P_\alpha)$ in table 5 for all 21 channels.

Table 5 In-band Scan- + Primary mirror thermal signals

Detector channel	E^{TOT}_{α} Thermal signal from scan+primary mirrors (10^{-8} watt)	S_{α} Maximum Expected in-band signal (10^{-8} watt)	$E^{TOT}_{\alpha}/S_{\alpha}$ mirror signal/ max.atmospheric signal	$E^{TOT}_{\alpha}/S_{\alpha}*(R_{\alpha}/NEN_{\alpha})$ mirror signal/ min. atmospheric signal
1	0.928	4.69	0.20	368
2	0.615	1.89	0.33	466
3	1.143	3.44	0.33	906
4	1.233	3.99	0.31	971
5	0.931	3.31	0.28	1016
6	0.482	5.41	0.09	1208
7	0.585	6.49	0.09	1377
8	1.339	15.26	0.09	3081
9	0.496	5.33	0.09	1129
10	0.487	3.14	0.16	1579
11	1.104	3.14	0.35	2158
12	0.388	2.57	0.15	1815
13	0.301	1.89	0.16	1295
14	0.452	1.66	0.27	1915
15	0.341	0.68	0.50	1454
16	0.257	0.40	0.64	1105
17	0.524	0.98	0.53	2031
18	0.462	0.91	0.51	1827
19	0.128	0.32	0.40	462
20	0.951	1.23	0.77	2791
21	0.277	0.34	0.81	1179

Table 4 shows that the direct, in-fov mirror thermal signals onto the detectors is expected to be lower than but generally still of the same order of magnitude as the maximum in-band signals expected from the atmosphere.
Column 5 in table 5, giving the ratio of the in-FOV mirror thermal signal to the in-band NEN signal values in each channel, shows that the in-fov (and therefore chopped) mirror thermal signal exceeds the NEN signal values by factors ranging from 370 to 3100. This implies that at times the instrument is intended to be able to measure accurately (to ≅ 1 NEN) a signal from the atmosphere which is as small as 1/3100 th part of an expected superimposed mirror thermal signal which cannot be removed by the HIRDLS chopping scheme.

10.0 Earth + structure thermal emission scattered from mirrors

A further source of background which must be considered is thermal emission from the OFOV Earth or OFOV spacecraft surfaces scattered from the mirrors. This contribution arises because even though a part of the Earth's or a spacecraft's surface may not be viewable from the detector via a **specular reflection (i.e. it is OFOV)** it may still be 'seen' via an **off-specular scattered path** (i.e. radiation from it can be scattered into the detector's FOV). The size of such contributions is proportional to the probability of scatter at a given angle from the specular direction which takes a ray from an emitting OFOV surface element to the detector via one or more mirror surfaces. The estimation of the scatter contribution to the signal background involves a construction similar to that shown in figure 3 except that the emission from surrounding surface elements falls initially onto a mirror surface element instead of the detector. Fig 6 shows the scheme.

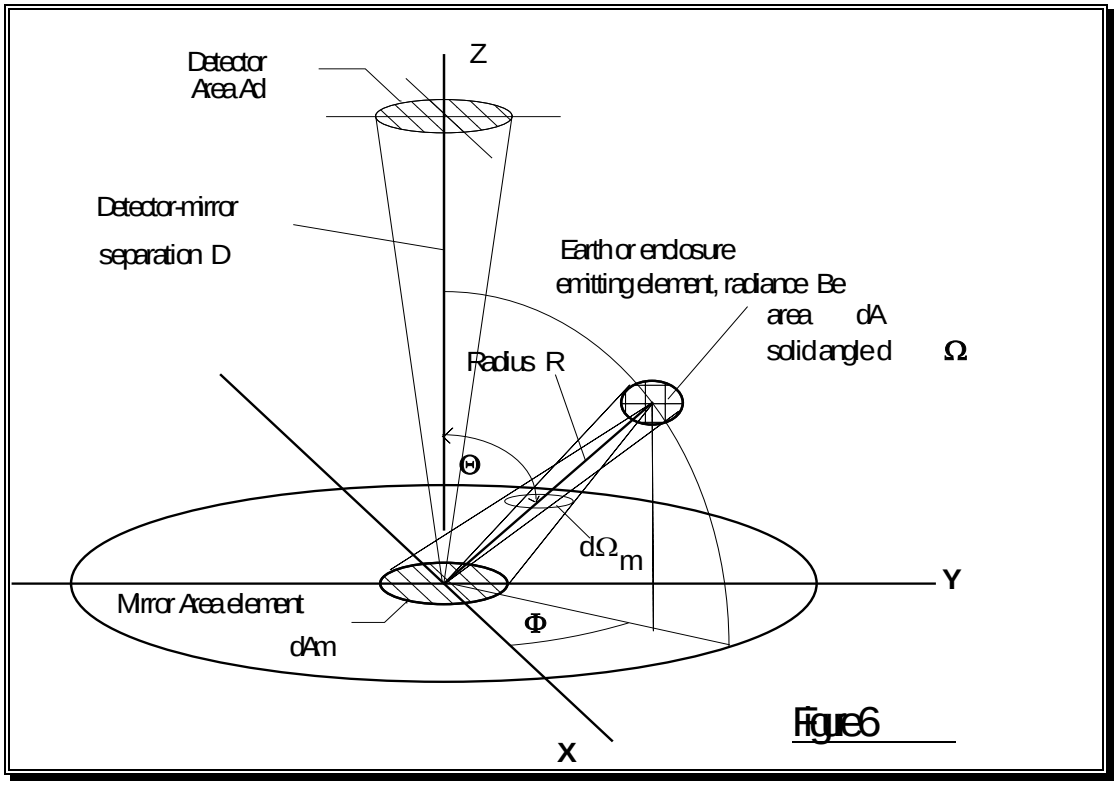

Figure 6

In order to proceed, we must introduce here the mirror BRDF or Bi-directional Reflection Distribution Function which describes the angular distribution and intensity of reflected incident light. It will here be given the symbol **BRDF(θ_i,φ_i;θ_s,φ_s),** where θ_i,φ_i,θ_s,φ_s are angles which define the incident and scattered light directions. If E is the intensity of collimated radiation incident (in watts/m^2) onto a unit area of scattering surface, then the intensity dE_{scat} (also in watts/m^2) scattered into a solid angle dΩ is given by

$$dE_{scat} = E.BRDF(\theta_i, \varphi_i; \theta_s, \varphi_s)d\Omega \qquad (15)$$

We can use equations (8)→(12) to estimate E, this time substituting the mirror area element dA_m for the detector area A_d. The solid angle **dΩ** in eq. (15) is just given by

$$d\Omega = A_d / D^2 \qquad (16)$$

The expression for dE_{scat} becomes

$$dE_{scat} = \int_{\theta_{min}}^{\theta_{max}} \int_0^{2\pi} B_e dA_m \left(\frac{A_d}{D^2}\right) BRDF(\Theta, \Phi; 0, 0) \sin\Theta \cos\Theta d\Theta d\Phi \qquad (17)$$

Summation over the mirror area results in

$$E_{scat} = B_e A_m \left(\frac{A_d}{D^2}\right) \int_{\theta_{min}}^{\theta_{max}} \int_0^{2\pi} BRDF(\Theta, \Phi; 0, 0) \sin\Theta \cos\Theta d\Theta d\Phi \qquad (18)$$

In eq.(18), A_m is the mirror area visible to the detector and A_d/D^2 is just the solid angle subtended by the detector at the visible mirror area. B_e , the radiance of the enclosure surface, is given by eq. (6) as before.

10.1 An important assumption

It is important to note that to get eq. (18), a simplifying approximation has been made deriving eq.(17) whereby the values of the angles **Θ** and **Φ** for each mirror element dA_m have been replaced by mean values exactly applicable only to the central element, for which (θ_s,ϕ_s) = (**0,0**). This will be a good approximation for the flat scan-mirror, given the very small solid

angle that it subtends at the prime focus detector position. It can be shown to be a reasonable approximation for the curved primary mirror given the relatively small (11/2 degrees) angle of tilt between the normal to a peripheral mirror element and the normal to the axial element (see fig 4).

Integration of eq.(18) requires knowledge of the angular dependence of **BRDF(Θ,Φ,0,0)** with Θ= the angle of scatter from the specular direction**.** Here we use a generally-accepted approximate form for BRDF**:**

$$BRDF(\Theta,\Phi) = C_1.\Theta^{-C_2} + C_3\Psi\exp(-C_4\Theta) \qquad (19)$$

The first term models scatter from the general surface roughness (or 'topographic' scatter) and the second term models scatter from particulate and other contamination. The quantity **Ψ** is a measure of the amount of obscuration of the mirror's surface by contamination. (Typical values for the 5 parameters C_1,C_2,C_3,C_4 and Ψ will be quoted later when calculations are done). It is noted that, frequently, measurements of the BRDFs of contaminated mirrors can be fitted well, over a reasonably wide angular range, by the functional form of the first term. The BRDF difference between a pristine and a contaminated mirror surface then shows up as an increase in the C_1 value and a change (usually a reduction) in the logarithmic slope C_2 compared to the uncontaminated case.

The integral in eq. (18) with eq. (19) substituted for BRDF(Θ,Φ) becomes

$$E_{scat} = B_e A_m \left[\frac{A_d}{D^2}\right] \int_{\Theta_{min}}^{\Theta_{max}} \int_0^{2\pi} \left(C_1.\Theta^{-C_2} + C_3\Psi\exp(-C_4\Theta)\right) \sin\Theta\cos\Theta d\Theta d\Phi \qquad (20)$$

A minimum value Θ_{min} is specified in the integral in order to avoid including the specular direction (where the integrand may diverge if certain fitted BRDF angular behaviour is extrapolated to Θ = 0) and to represent the normal situation where a mirror has a clear FOV (containing no structure) having a certain angular size. Equation(20) can be rewritten

$$B_{scat}(\Theta_{min},\Theta_{max}) = \frac{E_{scat}(\Theta_{min},\Theta_{max})}{\left(A_d/D^2\right)A_m} = B_e\left(I_{top} + I_{cont}\right) = B_e I_{scat}(\Theta_{min},\Theta_{max}) \qquad (21)$$

Equation (21) defines an effective scatter radiance B_{scat} having the same units as the radiance B_e of the emitting surround. The two integrals I_{top} and I_{cont} define two **<u>fractions</u>** of the scatter radiance, namely a 'topographic scatter' fraction from residual surface roughness and a 'contamination scatter' fraction from particles contaminating the surface. The first integral involves the product of the functions $\sin(\Theta)/\Theta^{C_2}$ and cosΘ. It cannot be integrated analytically for non-integral C_2 but accurate approximations exist[1] for both functions over the range 0<Θ<π/2 which enable integration. These are

$$\sin\Theta/\Theta^{C2} = (1 - 0.16605\Theta^2 + 0.00761\Theta^4)/\Theta^{C2-1}, \quad \cos\Theta = 1 - 0.4967\Theta^2 + 0.03705\Theta^4 \qquad (22)$$

with an error less than 0.001 over the range 0<Θ<π/2. If these functions are substituted into eq. (20), both integrals can be done analytically. The results for I_{top} is (with p=2-C_2)

$$I_{top}(\Theta_{min},\Theta\max) = 2\pi C_1\left[\frac{\Theta^p}{p} - 0.66275\frac{\Theta^2}{2+p} + 0.127137\frac{\Theta^4}{4+p} - 0.009932\frac{\Theta^6}{6+p} + 0.00028195\frac{\Theta^8}{8+p}\right]_{\Theta_{min}}^{\Theta_{max}} \qquad (23)$$

This formula is OK (does not diverge) for $\Theta_{min} \to 0$ so long as p>0 (i.e. so long as C_2 <2). The integral of the second term in eq. (20) is accurately represented by the expression

$$I_{cont}(\Theta_{min},\Theta\max) = \frac{2\pi C_3\Psi}{(C_4^2+4)}\left[\cos 2\Theta + 0.5C_4\sin 2\Theta\right]e^{-C_4\Theta}\Big]_{\Theta_{min}}^{\Theta_{max}} \qquad (24)$$

Note that I_{cont} does not diverge for $\Theta_{min} \to 0$.

10.2 Typical mirror-scatter performance calculations

[1] Abramowitz and Stegun, 'Handbook of Mathematical Functions', eq. 4.3.96-99

With the angle Θ expressed in radians in eq. (19), a perfectly clean, polished mirror surface will be well represented by choosing the following values for C_1 and C_2 in the equation for the BRDF:

$$C_1 = 3.0 \times 10^{-6}, \quad C_2 = 1.7 \qquad (25)$$

With the angular behaviour chosen, these parameters give a BRDF (at Θ = 1 deg) = 2.9×10^{-3} . Super-polished mirrors can be achieved yielding a BRDF (at Θ = 1 deg) $\cong 3 \times 10^{-4}$ (ten times smaller) at λ = 10.6μ, with $C_2 \cong 2$. For now, the more conservative choice above for $C_1$and C_2 is kept for illustration.

Empirical values for C_3 and C_4 and formulae relating Ψ to exposure time at various air cleanliness levels can be found in reference 2. Reasonable values for a very lightly dust-contaminated mirror might be[2]

$$C_3 = 8.4, \quad C_4 = 4.0, \quad \Psi = 1.6 \times 10^{-5} \qquad (26)$$

The value selected for Ψ represents surface contamination at a level of class 150 **surface** cleanliness with an assumed particle-size distribution i.e. the surface is a **class 150 surface**. This level is reached by exposure of the originally clean surface to air of a given cleanliness level over a length of time[3] which is shorter the dirtier the air (the larger the air class number). Note that the BRDF model related to air class is critically dependant on the actual particle-size distribution present in the contaminating air. A 'standard' measured distribution has been used to get the quoted Ψ value.

Surface scatter depends on some power of the wavelength λ of the scattered radiation , so the 'constants' C_1 and C_3 are in general λ-dependant. The values quoted are typical for a wavelength of 10.6 μm (approximately midway through the waveband covered by the HIRDLS detectors).

Equations (23) and (24) have been evaluated to give $I_{scat}(\Theta_{min}, \Theta_{max})$ for $\Theta_{min} = 2 \rightarrow 40$ deg at 2 deg (0.035 rad) intervals and for a single value for Θ_{max} = 90 deg. Table 6 shows the results. Table 6 values indicate the levels of scatter to expect at a detector from a mirror, assuming that the mirror 'looks through' apertures in the structure which keep clear of conical FOVs having half-cone angles ranging from 2 to 40 degrees and assuming that it views structure over the rest of the solid angle in front of it. The table shows that, in such a situation, particulate scatter from even a very clean surface given only a short exposure to very well filtered air can soon exceed the scatter from the remaining surface roughness.

---

[2] Muscari,J.A., Proc. SPIE,Vol 675(1986)

[3] e.g., for a vertical surface, class 150 cleanliness is reached after 2.9 hours exposure to class 1000 air or 18.6 hours of class 100. The formula used is $\log_{10}$(hours exposure) = 0.926 ($\log_{10}$(class surface))^2 - 0.773 $\log_{10}$(class room air) - 1.57. All particles assumed > 5 micron diameter. see 'Particulate contamination control', Muscari,J.A., Proc. SPIE,Vol 675(1986)

Table 6 Topographic and particulate scatter fractions from a mirror surround extending from Θmin to 90 deg from boresight

topographic scatter parameters		contamination scatter parameters	
C_1= 3.0x 10^{-6} C_2= 8.40		C_3= 1.70, C_4= 4.00 Ψ= 1.6x10^{-5} (class 150 air)	
	Itop fraction	Icont fraction	Iscat
Θ_{min} (deg)	(topographic)	(contamination)	
2	3.704*10^-5	4.175*10^-5	7.880*10^-5
4	3.174*10^-5	4.051*10^-5	7.226*10^-5
6	2.810*10^-5	3.872*10^-5	6.682*10^-5
8	2.525*10^-5	3.653*10^-5	6.179*10^-5
10	2.288*10^-5	3.411*10^-5	5.699*10^-5
12	2.084*10^-5	3.155*10^-5	5.239*10^-5
14	1.904*10^-5	2.895*10^-5	4.799*10^-5
16	1.744*10^-5	2.636*10^-5	4.380*10^-5
18	1.598*10^-5	2.385*10^-5	3.983*10^-5
20	1.466*10^-5	2.144*10^-5	3.610*10^-5
22	1.345*10^-5	1.917*10^-5	3.261*10^-5
24	1.233*10^-5	1.704*10^-5	2.937*10^-5
26	1.129*10^-5	1.507*10^-5	2.636*10^-5
28	1.034*10^-5	1.326*10^-5	2.359*10^-5
30	9.449*10^-6	1.161*10^-5	2.105*10^-5
32	8.623*10^-6	1.011*10^-5	1.873*10^-5
34	7.854*10^-6	8.766*10^-6	1.662*10^-5
36	7.138*10^-6	7.562*10^-6	1.470*10^-5
38	6.473*10^-6	6.492*10^-6	1.296*10^-5
40	5.853*10^-6	5.544*10^-6	1.140*10^-5

It is useful to compare table 6 values with expected noise levels in the HIRDLS channels. To do this we invert the numbers in column 10 in table 3 for the ratio $\mathbf{B_\alpha(300)/NEN_\alpha}$ to get $\mathbf{NEN_\alpha / B_\alpha(300)}$. These form column 4 in table 7 and they can be compared with the biggest total scatter fraction total $I_{scat}(\Theta_{min}, 90)$ taken from table 6 for Θ_{min} = 2 deg., both uncorrected for wavelength dependence (col. 5) and corrected for an assumed $1/\lambda^2$ wavelength behaviour (col. 6), normalising to the channel 9 value (which is nearest to 10.6μ, the wavelength at which the quoted scattering parameters C_1 and C_3 apply). Also taken from table 6 and given in cols. 7 and 8 are unscaled and scaled total scatter fractions for Θ_{min} = 30 deg.

Table 7 Wavelength-scaled mirror scatter compared with in-band noise radiances

Detector channel	λmean (μ)	$(10.6/\lambda)^2$ scale factor	$\mathbf{NEN_\alpha / B_\alpha(300)}$	Iscat(2) (no scale factor)	Iscat(2) (with scale factor)	Iscat(30) (no scale factor)	Iscat(30) (with scale factor)
1	17.38	0.37	31.94*10^-5	7.880*10^-5	2.92*10^-5	2.105*10^-5	0.78*10^-5
2	16.47	0.41	25.28*10^-5	7.880*10^-5	3.23*10^-5	2.105*10^-5	0.86*10^-5
3	16.00	0.44	12.56*10^-5	7.880*10^-5	3.47*10^-5	2.105*10^-5	0.93*10^-5
4	15.56	0.46	11.82*10^-5	7.880*10^-5	3.62*10^-5	2.105*10^-5	0.97*10^-5
5	14.99	0.50	11.49*10^-5	7.880*10^-5	3.94*10^-5	2.105*10^-5	1.05*10^-5
6	12.07	0.77	9.31*10^-5	7.880*10^-5	6.07*10^-5	2.105*10^-5	1.62*10^-5
7	11.85	0.80	8.17*10^-5	7.880*10^-5	6.30*10^-5	2.105*10^-5	1.68*10^-5
8	11.34	0.87	3.65*10^-5	7.880*10^-5	6.86*10^-5	2.105*10^-5	1.83*10^-5
9	10.82	0.96	9.96*10^-5	7.880*10^-5	7.56*10^-5	2.105*10^-5	2.02*10^-5
10	10.05	1.11	7.80*10^-5	7.880*10^-5	8.75*10^-5	2.105*10^-5	2.34*10^-5
11	9.58	1.22	5.41*10^-5	7.880*10^-5	9.61*10^-5	2.105*10^-5	2.57*10^-5
12	8.85	1.43	6.36*10^-5	7.880*10^-5	11.27*10^-5	2.105*10^-5	3.01*10^-5
13	8.26	1.65	8.83*10^-5	7.880*10^-5	13.00*10^-5	2.105*10^-5	3.47*10^-5
14	8.04	1.74	6.13*10^-5	7.880*10^-5	13.71*10^-5	2.105*10^-5	3.66*10^-5
15	7.88	1.81	7.99*10^-5	7.880*10^-5	14.26*10^-5	2.105*10^-5	3.81*10^-5
16	7.76	1.87	10.53*10^-5	7.880*10^-5	14.74*10^-5	2.105*10^-5	3.94*10^-5
17	7.42	2.04	5.67*10^-5	7.880*10^-5	16.08*10^-5	2.105*10^-5	4.29*10^-5
18	7.09	2.24	6.49*10^-5	7.880*10^-5	17.65*10^-5	2.105*10^-5	4.72*10^-5
19	7.10	2.23	24.76*10^-5	7.880*10^-5	17.57*10^-5	2.105*10^-5	4.69*10^-5
20	6.76	2.46	4.18*10^-5	7.880*10^-5	19.38*10^-5	2.105*10^-5	5.18*10^-5
21	6.22	2.90	9.82*10^-5	7.880*10^-5	22.85*10^-5	2.105*10^-5	6.10*10^-5

The table 7 results allow estimation of the expected **constant** level of mirror scatter onto a detector from a mirror having the **fixed** viewing geometry shown in figure 7. This geometry can be applied to the primary mirror as shown in figure. 8.

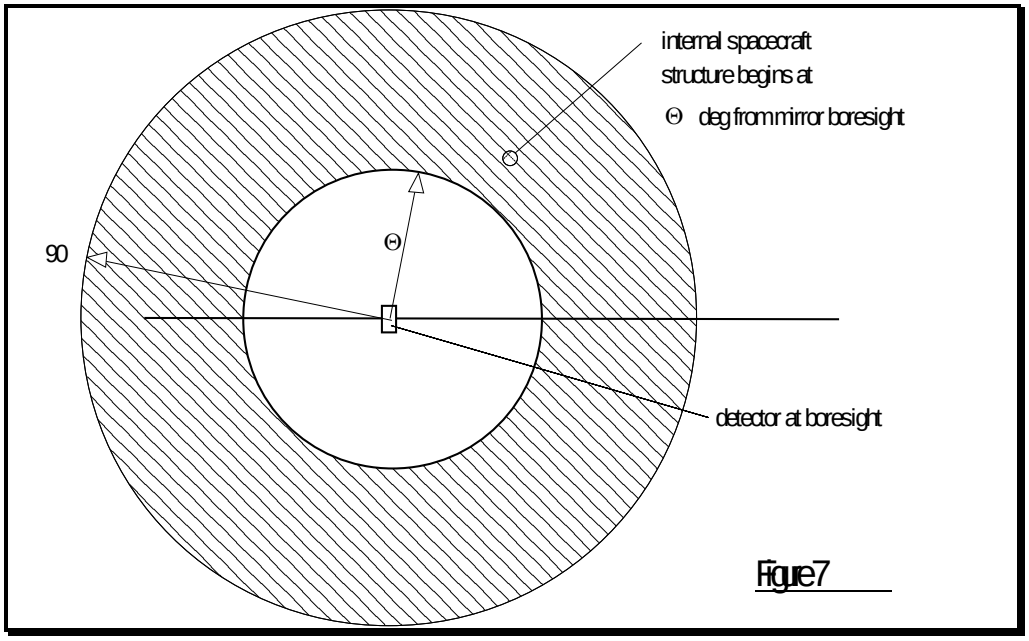

10.3 Primary mirror viewing geometry

With the parameters defined in figure 8, the Θ angle for the primary mirror's view of its surroundings excluding the scan-mirror aperture is given by

$$Tan\Theta = \frac{(D_p + D_S)}{S} \quad (27)$$

Taking Ds ≅ Dp = 170 mm and S ≅ 550 mm this give Θ ≅ 32 deg. Table 6 shows that, for this geometry, the scatter from structure outside the Θ = 32 deg cone is approximately one-quarter of the scatter expected if the structure extended from Θ = 2 deg . Table 7 shows that for this geometry, the scatter signal can be below the NEN radiance values in all channels.

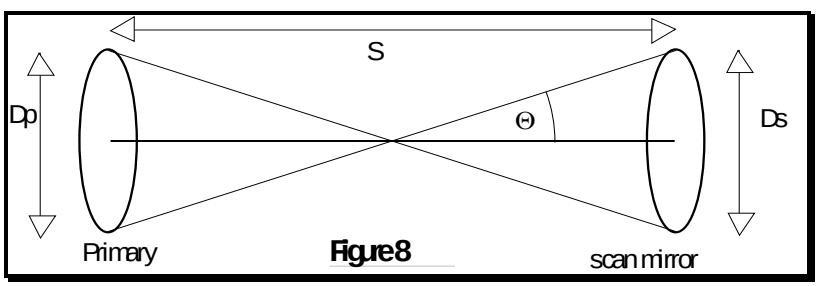

Because the scan mirror occupies a non-negligible portion of the primary mirror's FOV (a roughly 64 deg. cone), it is necessary to consider what structure the primary might see when viewing it in reflection from the scan-mirror i.e. what the primary might see through the 'aperture' that the scan-mirror represents. Before answering this question , the view of structure and earth that the scan-mirror 'aperture' has must be considered.

10.4 Scan-mirror viewing geometry

The scan-mirror views space, the earth's atmosphere **and the earth** through an aperture in the spacecraft structure which is wide in the azimuthal scan direction and narrower in the vertical scan direction. Therefore the FOV that the scan-mirror aperture has would have roughly the proportions shown in figure 9.

It is emphasised that the **aperture** of the scan-mirror sees a **fixed** view of structure and the earth, since the **location** of the scan-mirror aperture remains fixed relative to the spacecraft structure (the angles of incidence from structure onto the scan-

mirror do change however and the aperture's projected area in a given direction will therefore vary somewhat with scan angle).

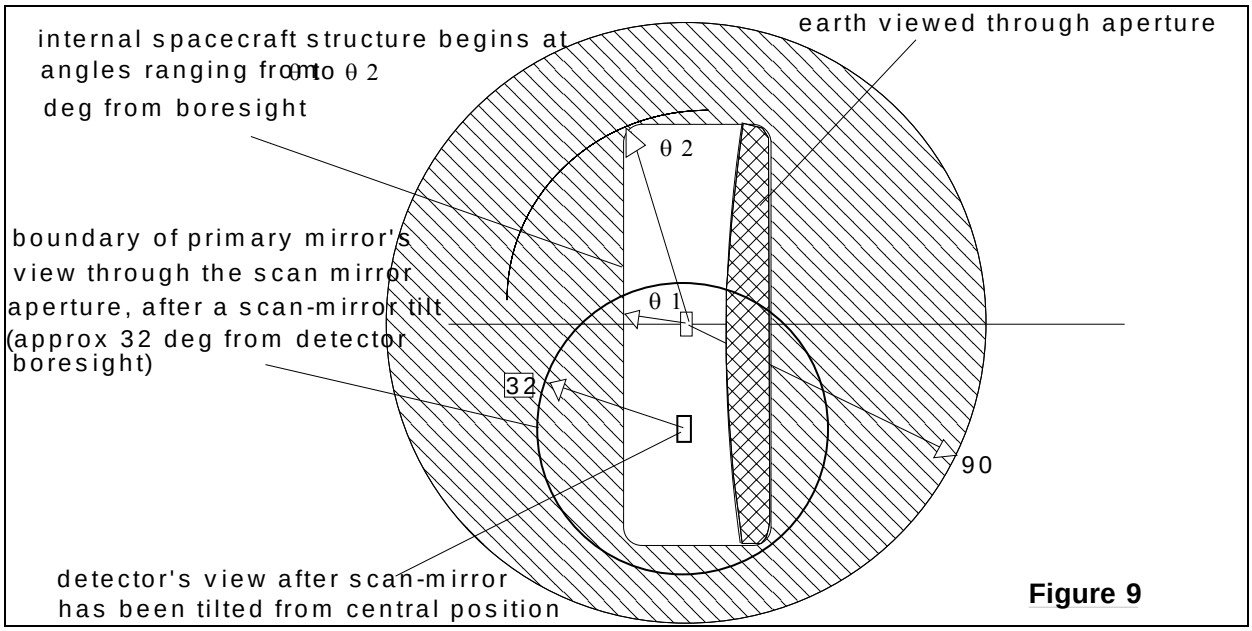

Figure 9

To complicate things, both the detector's view and the primary mirror aperture's view through the scan-mirror are actually moved relative to the scan-mirrors 'view' when the scan mirror tilts away from its mean position (to cause the detector to view a different part of the earth's atmosphere). In figure 9 the simultaneous change in the detector's boresight location and the centre of the primary mirror's view as a result of an azimuthal angular movement is shown relative to the fixed scan-mirror aperture's view. Their new locations are indicated schematically with thick lines. The positions of the detector boresight and primary mirror aperture's view remain fixed relative to each other.

The motion of a mirror's 'view' relative to structure and the earth as the scan-mirror steps the detector's view to a new position will result in a change in the signal due to scatter from the mirror of structure- and earth-emitted radiation. This variation in the scatter signal will be a problem if it is relatively large since it will prevent accurate calibration of the scatter signal by moving the detector's view out to space (i.e. to a height above the earth's limb where the atmospheric signal can be considered to have fallen to zero) in order to measure the residual scattered signal. An estimate will be made of the magnitude to be expected for these variations

11.0 Variation in the mirror-scattered radiances due to viewing geometry variations

11.1 Simplified geometry for order-of-magnitude calculations of scattered-signal variations

The levels of scattered radiation expected in a complicated viewing geometry as presented by HIRDLS cannot be accurately analysed without the use of powerful analysis packages such as APART and ASAP. However, some idea of the sizes of scatter signals can be obtained if a simpler geometry, such as that shown in figure 10, is studied. Results obtained can be related to those expected in the more complicated geometries that occur in practice in the HIRDLS instrument. Figure 10 represents a situation where a mirror 'sees' structure from angle Θ_{min} to angle Θ_{max} measured from the boresight and where the detector is located at the boresight. The earth's disk falls partially within the clear cone defined by Θ_{min} and it is represented with a straight-edged boundary (i.e. its curvature is ignored).

Because of HIRDLS height-scanning capability, the detector position can be moved over a range of angles which can take it onto the disk and up to an angular equivalent of 100 km or so above the disk (100 km = 1.9 degrees). What must be estimated is the scattered fraction of the radiance emitted by the part of the earth's disk viewed (this will be referred to here as $I_{earth}(\Theta<\Theta_{min},\Delta)$) plus the scattered fraction of the radiance emitted from the structure viewed between the two Θ - limits (which will be referred to as $I_{struc}(\Theta_{min},\Theta_{max})$).

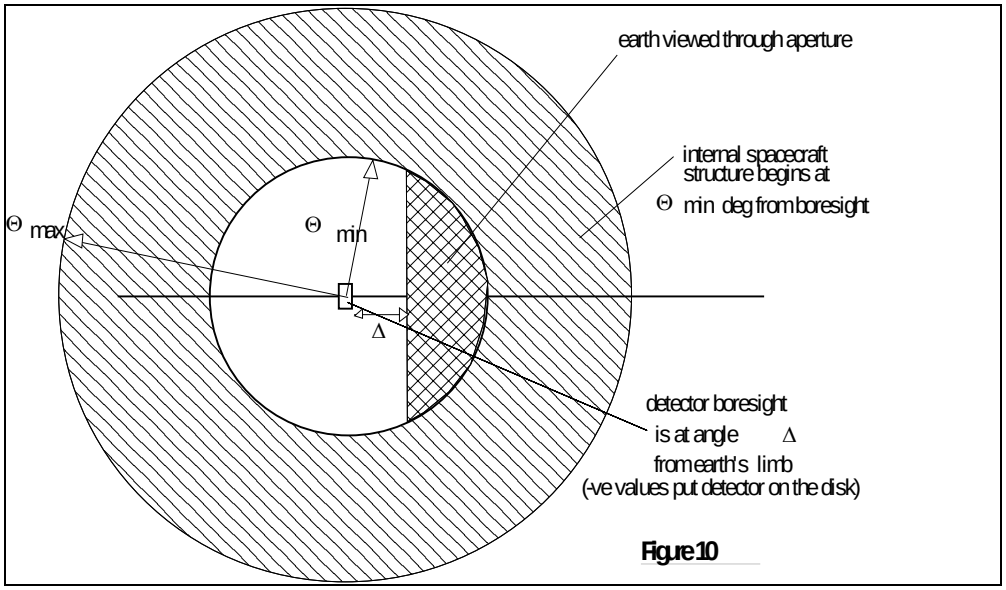

Figure 10

Equation (21) can be used to calculate the latter fraction, but numerical integration is needed to estimate the fraction scattered from areas of the partially-viewed earth, $I_{earth}(\Theta<\Theta_{min},\Delta)$. When calculating the scatter into the detector when the latter is viewing part of the earth's disk ($\Delta < 0$), the solid angle covered by the detector must be excluded from the region of integration, because we are interested in estimating scatter **into** the FOV (the detector area) from radiation coming from regions **outside** the FOV (this also helps us avoid the problem which can arise with the use of $\Theta_{min} = 0$ in eq. (23)). For this purpose a 2 km diameter circular area was excluded from all integrals.

Calculations of I_{earth} and I_{struc} for a range of detector locations Δ relative to the earth's limb were made using Θ_{min} = (5 deg $\rightarrow$ 45 deg in 5 deg steps) for Θ_{max} = 90 deg (tables 8A-8I) and Θ_{min} = (5 deg $\rightarrow$ 30 deg in 5 deg steps) for Θ_{max} = 32 deg (tables 9A-9F). For each Θ_{min} value, the range chosen for Δ was from -20 km (on the disk) to +100 km in 5 km steps. Equation (19) was used for the BRDF with the parameters given in eqs. (25) and (26) inserted. The tables are given in appendix A, for convenience.

Tables 8A-8I can be used to estimate scatter from the scan mirror, tables 9A-9F can be used to estimate scatter by the primary of radiation from surfaces seen in reflection from the scan-mirror. Table 6 can be used to estimate the component of scatter from the primary of radiation from outside the scan-mirrors area (as is done in table 7, column 8).

Tables 8 and 9 show importantly how the scattered signal can vary with detector LOS height above the earth's limb. The component I_{earth} varies slowly when the detector position is inside the earth's limb and when it is well (>60-70 km) outside. Overall, this component can vary by typically 50% or more (depending on Θ_{min} value) as one moves from disk to 100 km LOS height. However, when the fixed structure radiation scattered component is added to I_{earth} , the percentage change drops somewhat, but it can still be $\cong$ 30 % (depending on the (Θ_{min},Θ_{max}) values) between the two LOS extremes.

The tables can be used in the following way. Suppose that the scan-mirror's FOV inner-boundary is formed by structure between (see figure 9) Θ-values Θ_1=15 deg and Θ_2=45 deg from its boresight direction. The assumption is then made that a reasonable estimate of the scatter to be expected from structure extending from this boundary out to Θ_{max} = 90 deg (and from earth viewed within the boundary) can be made by taking the mean of the scatter resulting from using the figure 10 geometry with, respectively,Θ_{min} =15 deg and Θ_{min} = 45 deg and Θ_{max} = 90 deg for both. Thus, since table 8C gives estimates for scatter using (Θ_{min}=15,Θ_{max} =90) and table 8I gives estimates for scatter using (Θ_{min}=45,Θ_{max} =90), the column 4 values in the two tables can be averaged to give an estimate.

It is more complicated to estimate the scatter from the structure and earth within the part of the scan-mirror FOV that the primary can see in reflection through the scan-mirror, because the primary can see only such structure as lies within approximately 32 degrees of the boresight (see figure 8), so table 9 values (which use $\Theta_{min} < \Theta_{max}$ = 32 deg) do not exist for Θ_{min} = 45 deg. However, the values in all such tables having $\Theta_{min} > \Theta_{max}$ = 32 deg would be zeros, so the average of two tables becomes equal to one-half the values in the table for Θ_{min} = 15 deg . A best-estimate is therefore taken to be the column 4-values in table 9C divided by 2 (we will assume scan-mirror reflectivity = 1.0). **<u>All the above calculations assume equal 300K blackbody temperatures for the structure and earth and emissivities = 1</u>**.

Table 10 shows the result of combing one-half of the column 4 values in each of tables 8C and 8I with one-half of the column 4 values in table 9C and adding the column 4 value in table 6 for Θ_{min} = 32 deg. These numbers represent channel 10 values ($\lambda_{mean} \cong 10\ \mu$). To obtain numbers representative of the other channels, the table 10 values should be multiplied by the wavelength-scaling factors given in column 3 of table 7.

Table 10 Estimated Mirror-scattered radiances in channel 10 as fractions of earth/structure radiances as a function of LOS height (km)

Δ (km)	Iearth	Istruc	Iearth+Istruc
-20.0	5.45*10^-5	5.94*10^-5	11.39*10^-5
-15.0	5.33*10^-5	5.94*10^-5	11.27*10^-5
-10.0	5.19*10^-5	5.94*10^-5	11.13*10^-5
-5.0	4.98*10^-5	5.94*10^-5	10.92*10^-5
0.0	4.75*10^-5	5.94*10^-5	10.69*10^-5
5.0	4.24*10^-5	5.94*10^-5	10.18*10^-5
10.0	4.04*10^-5	5.94*10^-5	9.98*10^-5
15.0	3.89*10^-5	5.94*10^-5	9.83*10^-5
20.0	3.77*10^-5	5.94*10^-5	9.71*10^-5
25.0	3.68*10^-5	5.94*10^-5	9.62*10^-5
30.0	3.59*10^-5	5.94*10^-5	9.53*10^-5
35.0	3.51*10^-5	5.94*10^-5	9.45*10^-5
40.0	3.44*10^-5	5.94*10^-5	9.38*10^-5
45.0	3.37*10^-5	5.94*10^-5	9.31*10^-5
50.0	3.31*10^-5	5.94*10^-5	9.25*10^-5
55.0	3.25*10^-5	5.94*10^-5	9.19*10^-5
60.0	3.19*10^-5	5.94*10^-5	9.13*10^-5
65.0	3.14*10^-5	5.94*10^-5	9.08*10^-5
70.0	3.09*10^-5	5.94*10^-5	9.03*10^-5
75.0	3.04*10^-5	5.94*10^-5	8.98*10^-5
80.0	3.00*10^-5	5.94*10^-5	8.94*10^-5
85.0	2.95*10^-5	5.94*10^-5	8.89*10^-5
90.0	2.91*10^-5	5.94*10^-5	8.85*10^-5
95.0	2.87*10^-5	5.94*10^-5	8.81*10^-5
100.0	2.83*10^-5	5.94*10^-5	8.77*10^-5

The above values are comparable to the $NEN_\alpha/B_\alpha(300)$ value of 7.8x10-5 for channel 10 given in table 7.

Because the primary's view through the scan-mirror is complicated when the latter is scanned azimuthally, the variation of this signal with azimuthal scan angle cannot be sensibly estimated without the use of APART with an accurate physical model of the HIRDLS optical front end, so it will not be attempted here.

12.0 Estimating Diffraction effects

Diffraction calculations are very difficult. In order to get quick estimates of diffraction effects, one is forced to use formulae for one of the very few cases which yield an analytical solution e.g. the case of a circular aperture illuminated by a plane wave along the axis. Insofar as the optical system in question exhibits such cylindrical symmetry and such illumination conditions, then the use of the equation for the intensity distribution E(Θ) near an axial point will give a reasonable estimate of the diffraction effects. However, if the optical system exhibits diffraction from shadowed apertures and straight edges, such simplification will probably lead to large errors in the estimation of the diffraction effects.

12.1 The Airy diffraction formula

The well-known Airy solution for the intensity or energy distribution E(Θ) in the diffraction pattern near an axial point due to illumination of a circular aperture, diameter D, by a plane wave, wavelength λ, incident parallel to the axis of symmetry is given by (see fig. 11)

$$E(\Theta) = E_0 K \left[\frac{J_1(u)}{u}\right]^2 \quad (28a)$$

$u = \pi D \sin\Theta / \lambda$ (28b)

$\sin\Theta = h / R$ (28c)

In eq. (28a), K is a normalisation constant, $J_1(u)$ is the Bessel function of the first kind[4] of order 1.

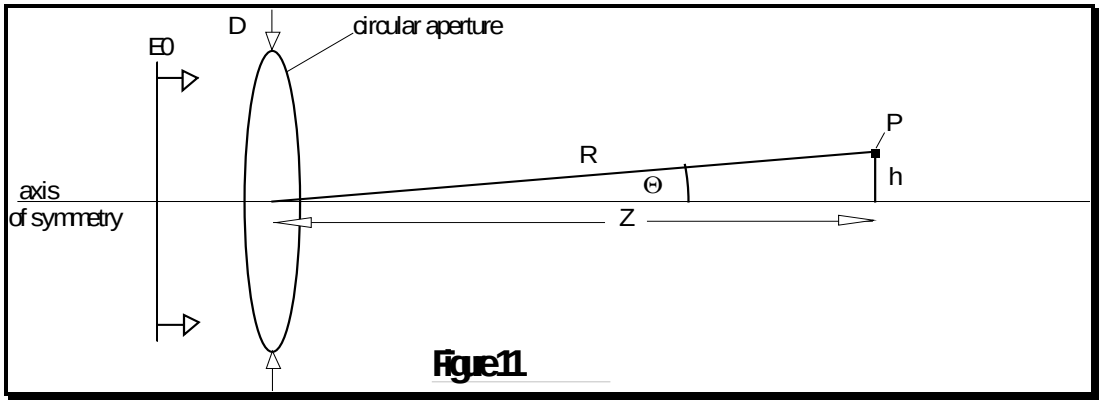

The above equation gives the Fraunhofer approximation i.e. the 'far-field' solution to the Kirchhoff diffraction integral when R >> D. Such an approximation is valid for example when the image point P is in the focal plane of an lens or mirror which is located close behind the diffracting aperture. In this case R = ∞.

The equation is frequently applied to the situation shown in figure 12, where the light is incident at an angle Θ_i to the axis and he diffracted intensity is wanted at a point near the axis at an angular distance Θ from the incident direction. The use of the equation in this case is probably permitted so long as $\Theta_i << 1$ and $\Theta_i + \Theta << 1$.

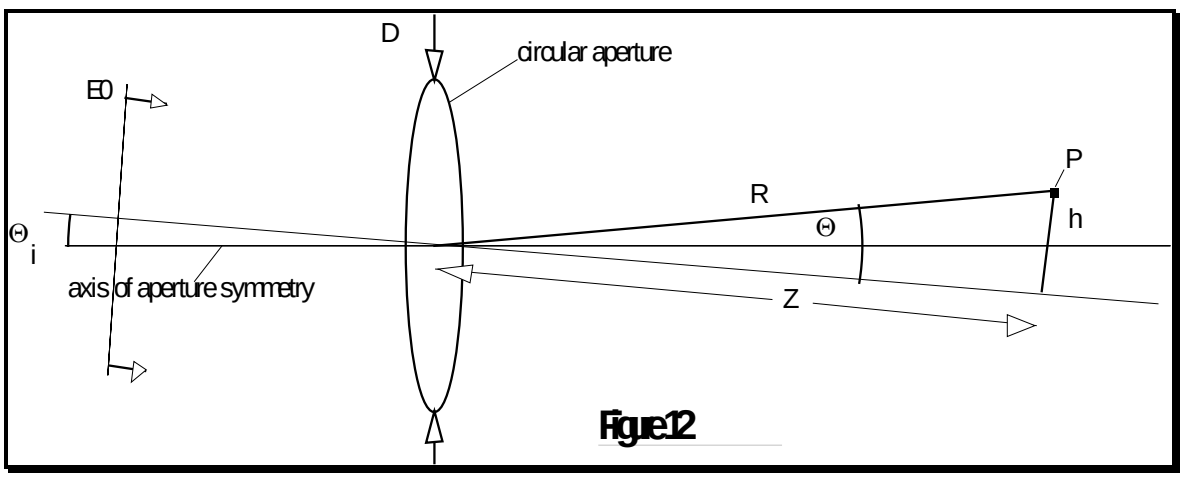

The Airy function eq. (28) decreases rapidly with increasing u-values after its first zero at u=1.22π. For D=170 mm and λ ≅ 10μ (values applicable to the median HIRDLS channel)

$\pi D / \lambda = 53407$ (29)

Using equations (29) and (28b)shows that the Airy function (and integrals involving it) contributes mainly to values of u where sinΘ<=7.18x10-5 sr = 14.8 arc.seconds. In this region, the approximation sinΘ ≅ Θ is very good, as it is even when u gets as large as 1000x1.22π, since Θ is only 4 degrees even then.

In order to use eq. (28), the normalisation constant K is needed. This is derived assuming unit energy or intensity in the incident beam and integrating eq. (28) over the whole of the diffraction pattern (see eq.(30)).

[4] Abramowitz and Stegun, 'Handbook of Mathematical Functions', chap.9

$$E_0 = 1 = \int_0^{2\pi}\int_0^{h_{max}} E(\Theta)\, h\,dh\,d\varphi \quad (30)$$

The following can be used to simplify eq. (30):

$$h\,dh = R^2 (h/R)(dh/R) = R^2 \sin\Theta\, d(\sin\Theta) = R^2 \left(\lambda/\pi D\right)^2 u\,du \quad (31)$$

Since the contribution to the integral in eq. (30) is dominated by contributions from u=πDsinΘ/λ<=1.22π, the upper limit to the u-integral can be extended to ∞ without incurring significant error. The result is

$$1 = KR^2 \left(\frac{\lambda}{\pi D}\right)^2 \int_0^{2\pi}\int_0^{\infty} \left(\frac{J_1(u)}{u}\right)^2 u\,du\,d\varphi \quad (32)$$

The following properties of Bessel functions can be used to do the u-integration [5]

$$J_1(u)/u = J_0 - \frac{dJ_1}{du} \quad (33)$$

$$J_1(u) = -\frac{dJ_0}{du} \quad (34)$$

$$\frac{\lim J_1(u)}{u \to \infty} = 0, \frac{\lim J_0(u)}{u \to \infty} = 0 \quad (35)$$

$$\frac{\lim J_1(u)}{u \to 0} = 0, \frac{\lim J_0(u)}{u \to 0} = 1 \quad (36)$$

Equation (32) then becomes

$$1 = KR^2 \left(\frac{\lambda}{\pi D}\right)^2 2\pi \left[-\tfrac{1}{2}\left(J_1^2 + J_0^2\right)\right]_0^{\infty} = K\pi R^2 \left(\frac{\lambda}{\pi D}\right)^2 \quad (37)$$

This gives K as

$$K = \frac{1}{\pi R^2}\left(\frac{\pi D}{\lambda}\right)^2 \quad (38)$$

Equation (28) can now be substituted by

$$E(\Theta)\,h\,dh\,d\varphi = \frac{E_0}{\pi R^2}\left(\frac{\pi D}{\lambda}\right)^2 \left(\frac{J_1(u)}{u}\right)^2 h\,dh\,d\varphi = \frac{E_0}{\pi}\left(\frac{\pi D}{\lambda}\right)^2 \left(\frac{J_1(u)}{u}\right)^2 \frac{h\,dh\,d\varphi}{R^2} = E_0 \frac{1}{\pi}\left(\frac{\pi D}{\lambda}\right)^2 \left(\frac{J_1(u)}{u}\right)^2 d\Omega \quad (39)$$

12.2 The Bi-directional Diffraction Distribution Function (BDDF)

Equation (39) shows that we can define a Bi-directional Diffraction Distribution Function I(Θ) (cf the mirror-scatter BRDF) for a circular aperture, given by

$$I(\Theta) = \frac{1}{\pi}\left(\frac{\pi D}{\lambda}\right)^2 \left(\frac{J_1(u)}{u}\right)^2 \quad (40)$$

with u given by eq. (28b). Some properties of the function in brackets in eq. (40) involving the variable **u** can be gleaned from the following accurate approximations [6]

---

[5] Abramowitz and Stegun, 'Handbook of Mathematical Functions', eqs (9.2.27)

[6] Abramowitz and Stegun, 'Handbook of Mathematical Functions', eq. (9.4.4,9.4.6)

$$\frac{J_1(u)}{u} = 0.5 - 0.556249985(u/3)^2 + 0.21093573(u/3)^4 - 0.03954289(u/3)^6 + 0.00443319(u/3)^8 - 0.00031761(u/3)^{10} + 0.00001109(u/3)^{12} \quad (41)$$

for $(u <= 3)$ and

$$\frac{J_1(u)}{u} = \frac{f_1(u)}{u^{\frac{3}{2}}}\cos(\theta_1) \quad (42)$$

for $(3 \le u < \infty)$, with

$$f_1(u) = \sqrt{2/\pi} + 0.00000156(3/u) + 0.01659667(3/u)^2 + 0.00017107(3/u)^3 - 0.00249511(3/u)^4 + 0.00113656(3/u)^5 - 0.00020033(3/u)^6 \quad (42a)$$

$$\theta_1(u) = u - 3\pi/4 + 0.12499612(3/u) + 0.0000565(3/u)^2 - 0.00637879(3/u)^3 + 0.00074348(3/u)^4 + 0.00079824(3/u)^5 - 0.00029166(3/u)^6 \quad (42b)$$

For large u, eq. (40) becomes

$$I(\Theta) = \frac{1}{\pi}\left(\frac{\pi D}{\lambda}\right)^2 \left(\frac{2/\pi}{u^3}\right)\cos^2(u - 3\pi/4) \quad (43)$$

If eq. (28b) is used for u and $\cos^2(u-3\pi/4) = (1/2)(1+\sin 2u)$ substituted, eq. (43) becomes

$$I(\Theta) = \frac{1}{\pi}\left(\frac{\pi D}{\lambda}\right)^2 \left(\frac{2/\pi}{(D\sin\Theta/\lambda)^3}\right)\frac{(1+\sin 2u)}{2} = \left(\frac{\lambda}{\pi^3 D\sin^3\Theta}\right)(1+\sin 2u) \quad (44)$$

In eq. (44), the term involving sin2u is sometimes neglected when integrations involving I(Θ) are carried out over Θ, reasoning that for large u, rapid oscillations induced in the integrand by the sin2u factor will result in little net contribution to the integral. Thus frequently I(Θ) is represented by the first term i.e.

$$I(\Theta) = \left(\lambda/\pi^3 D\sin^3\Theta\right) \quad (45)$$

For all diffraction calculations carried out here, the full expressions given by equations (41) and (42) were used.

12.3 Diffractive scatter estimates using the Airy BDDF

The BDDF I(Θ) can be used in eq.(18), just as were the mirror BRDFs, to estimate diffractive scatter contributions to the detectors. Tables equivalent to tables 8A-8I have been generated and they are given as tables 11A-11I (these are also relegated to appendix A for convenience). The geometry assumed is the same as before i.e. that shown in figure 10. Note that in the case of detector locations on the earth's disk, the diffractive scatter intensity must be computed by excluding the area of the detector from the integrals, as noted earlier. Table 11C is reproduced below as table 12 here in order to permit comparison with the table 10 values for mirror scatter derived earlier. Table 13 compares them.

Equation (45) shows a linear λ-dependence for the diffraction, so the totals given in tables 11 and 11A-11I for λ = 10μ can be simply scaled to other wavelengths. Thus the values in those tables should be roughly doubled to get values representative of channel 1 (17.4μ) and roughly halved to get channel 21 (6.2μ) values.

Table 13 already shows that the diffractive scatter fraction exceeds the surface scatter fraction by factors which vary with LOS height, by large factors at small heights and on the earth's disk and by smaller factors (nearer x2) at and beyond 60 km. Also note that whereas table 10 shows a substantial part of the mirror scatter fraction remaining constant with LOS height (possibly permitting it to be calibrated out), table 12 shows that a similar-sized diffractive scatter component which remains constant with height is a much smaller part of the total diffractive scatter fraction.

Table 12 Estimated Earth + structure diffraction radiances in channel 10 (λ = 10μ) as fractions of earth/structure radiances as a function of LOS height (km) above the 'limb'
(Θ_{min} = 15.0 deg , Θ_{max} = 90.0 deg)

LOS	Θ_{min} = 15.0 deg	**DIFFRACTION INTEGRALS**	Θ_{max} = 90.0 deg
Δ (km)	$I_{earth}(\Theta<\Theta_{min},\Delta)$	$I_{struc}(\Theta_{min},\Theta_{max})$	$I_{earth}+I_{struc}$,
-20.0	2.143*10^-2	3.588*10^-5	2.147*10^-2
-15.0	2.143*10^-2	3.588*10^-5	2.146*10^-2
-10.0	2.139*10^-2	3.588*10^-5	2.143*10^-2
-5.0	2.114*10^-2	3.588*10^-5	2.118*10^-2
.0	1.691*10^-2	3.588*10^-5	1.694*10^-2
5.0	2.007*10^-3	3.588*10^-5	2.043*10^-3
10.0	1.070*10^-3	3.588*10^-5	1.106*10^-3
15.0	7.157*10^-4	3.588*10^-5	7.515*10^-4
20.0	5.320*10^-4	3.588*10^-5	5.678*10^-4
25.0	4.250*10^-4	3.588*10^-5	4.609*10^-4
30.0	3.517*10^-4	3.588*10^-5	3.876*10^-4
35.0	2.981*10^-4	3.588*10^-5	3.340*10^-4
40.0	2.590*10^-4	3.588*10^-5	2.949*10^-4
45.0	2.282*10^-4	3.588*10^-5	2.641*10^-4
50.0	2.030*10^-4	3.588*10^-5	2.389*10^-4
55.0	1.829*10^-4	3.588*10^-5	2.188*10^-4
60.0	1.661*10^-4	3.588*10^-5	2.020*10^-4
65.0	1.515*10^-4	3.588*10^-5	1.874*10^-4
70.0	1.393*10^-4	3.588*10^-5	1.752*10^-4
75.0	1.287*10^-4	3.588*10^-5	1.646*10^-4
80.0	1.193*10^-4	3.588*10^-5	1.552*10^-4
85.0	1.111*10^-4	3.588*10^-5	1.469*10^-4
90.0	1.038*10^-4	3.588*10^-5	1.397*10^-4
95.0	9.726*10^-5	3.588*10^-5	1.331*10^-4
100.0	9.132*10^-5	3.588*10^-5	1.272*10^-4

Table 13 Estimated surface scatter + diffraction radiances in channel 10 (λ = 10 μ) as fractions of earth/structure radiances as a function of LOS height (km) above the 'limb'
(Θ_{min} = 15.0 deg , Θ_{max} = 90.0 deg)

LOS	**SURFACE SCATTER**	**DIFFRACTION**	**RATIO**
Δ (km)	$I_{earth}+I_{struc}$ (Iscat) Table 10	$I_{earth}+I_{struc}$ (Idiff) Table 12	DIFFRACTION/ SURFACE SCATTER
-20.0	11.39*10^-5	2.147*10^-2	188.50
-15.0	11.27*10^-5	2.146*10^-2	190.42
-10.0	11.13*10^-5	2.143*10^-2	192.54
-5.0	10.92*10^-5	2.118*10^-2	193.96
.0	10.69*10^-5	1.694*10^-2	158.47
5.0	10.18*10^-5	2.043*10^-3	20.07
10.0	9.98*10^-5	1.106*10^-3	11.08
15.0	9.83*10^-5	7.515*10^-4	7.64
20.0	9.71*10^-5	5.678*10^-4	5.84
25.0	9.62*10^-5	4.609*10^-4	4.79
30.0	9.53*10^-5	3.876*10^-4	4.07
35.0	9.45*10^-5	3.340*10^-4	3.53
40.0	9.38*10^-5	2.949*10^-4	3.14
45.0	9.31*10^-5	2.641*10^-4	2.84
50.0	9.25*10^-5	2.389*10^-4	2.58
55.0	9.19*10^-5	2.188*10^-4	2.38
60.0	9.13*10^-5	2.020*10^-4	2.21
65.0	9.08*10^-5	1.874*10^-4	2.06
70.0	9.03*10^-5	1.752*10^-4	1.95
75.0	8.98*10^-5	1.646*10^-4	1.83
80.0	8.94*10^-5	1.552*10^-4	1.74
85.0	8.89*10^-5	1.469*10^-4	1.65
90.0	8.85*10^-5	1.397*10^-4	1.58
95.0	8.81*10^-5	1.331*10^-4	1.51
100.0	8.77*10^-5	1.272*10^-4	1.45

12.4 Additional complications to diffraction estimates

As noted in the above section, the geometry assumed for all the calculations so far (including the diffraction calculations) is that of figure 10, where a uniform earth radiance is assumed **and zero radiance is assumed for the atmosphere above the earth's limb**. Thus there is a sharp cut-off (to zero) assumed in the radiance of the 'earth' at the geometrical edge of the earth. However, the atmosphere has finite radiance of course (since HIRDLS is intended to measure this!) and the figures B1-B21 given in appendix B show this. The figures are reproductions of the fiducial atmospheric radiance profiles in all 21 channels provided in TC-HIR-90 and computed by Chris Halvorsen of NCAR.

Complications arise because the integrals carried out to obtain the numbers given in all the tables so far (including tables 11 and 12) ignore the effects of this atmospheric emission on the radiance expected in the detector's FOV when the latter is located at a LOS height Δ above the geometrical earth's limb. Figure 11 shows what has been computed and figures 12 and 13 show two examples of what should be computed.

Integrations made assuming the geometry given in figure 10 can be simply illustrated as follows. Assume a finite detector width $\boldsymbol{\delta_d}$ in the height direction located to view the atmosphere element at height $\boldsymbol{\Delta}$ outside the earth's limb. Figure 11 shows one dimension of the two-dimensional integral which must be performed.

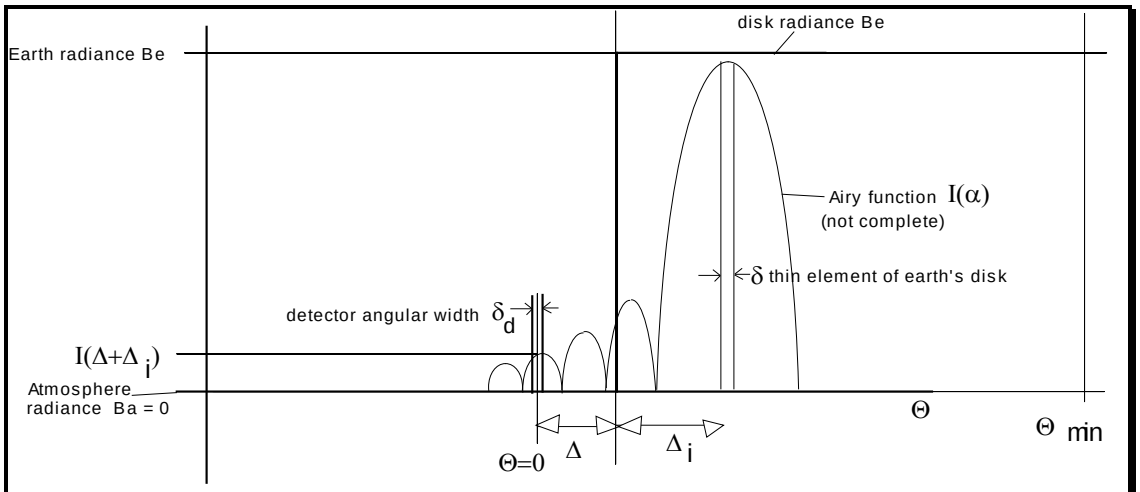

Figure 11 Zero atmospheric radiance case

With the symbols defined in figure 11, the signal dS (in watt/unit area of telescope aperture) entering the detector due to the radiance of an infinitesimal element $\boldsymbol{\delta}$ of the earth's disk located at distance $\boldsymbol{\Delta_i}$ inside the edge of the earth is given by (in one dimension only)

$$dS = (B_e \delta) \sum_{\Delta_i = 0}^{\Theta_{min}} I(\Delta + \Delta_i) \delta_d \quad (46)$$

The dimensionless fractional radiance $I_{diff}(\Delta)$ within the FOV of the detector at height $\boldsymbol{\Delta}$ is given by

$$I_{diff}(\Delta) = \frac{dS}{B_e \delta_d} = \delta \sum_{\Delta_i = 0}^{\Theta_{min}} I(\Delta + \Delta_i) \quad (47)$$

The summation in this case does not involve elements with **non-zero radiance** for which $\Delta + \Delta_i = 0$, as long as the detector position $\Delta > 0$ (i.e. is outside the region of non-zero radiance). Although diffraction is treated in eq. (47), the equation can just as easily apply to surface scatter if the mirror BRDF is substituted for the Airy BDDF.

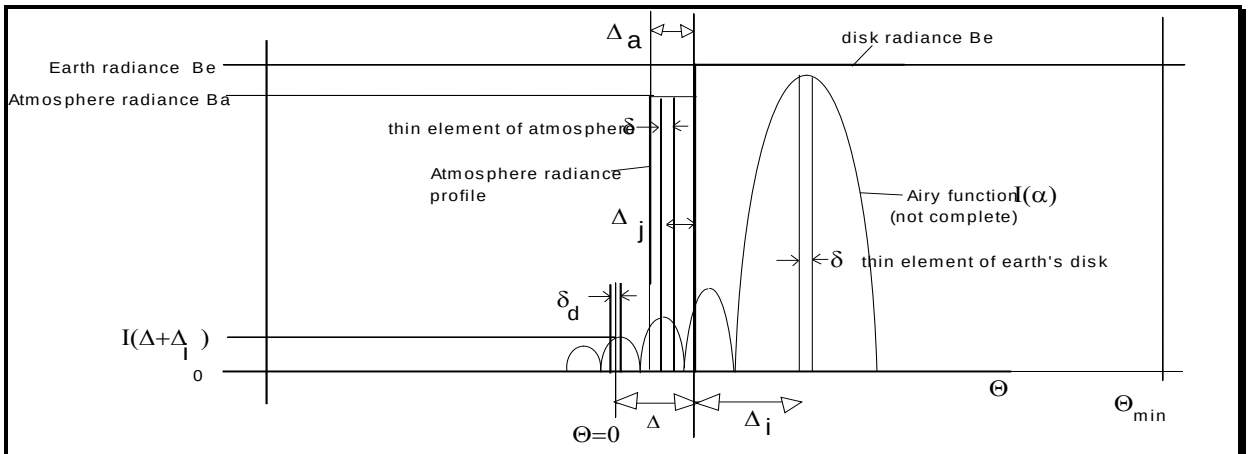

Figure 12 'Flat-topped' atmospheric radiance profile case

The equivalent integration for an atmospheric radiance profile of the shape shown in figure 12 (constant radiance = B_a with height out to an altitude $\Delta_{max} = \Delta_a$) is given by

$$I_{diff}(\Delta) = \frac{dS}{B_e \delta_d} = \delta \left[\sum_{\Delta_i=0}^{\Theta_{min}} I(\Delta + \Delta_i) + \left(\frac{B_a}{B_e} - 1 \right) \sum_{\Delta_j=0}^{\Delta_a} I(\Delta - \Delta_j) \right] \quad (48)$$

For detector heights $\Delta > \Delta_a$,the second summation does not involve elements for which $\Delta - \Delta_j = 0$ if the atmospheric radiance profile is as shown in figure 12. However, for detector heights $\Delta <= \Delta_a$, the second summation would involve elements for which $\Delta - \Delta_j = 0$. For these, we must exclude those elements from the summation which fall within a height range of +- 2.0 km from the detector centre, since this region is defined (see HIRDLS ITS para # 4.3.2) as being 'within the FOV' (even though each detector is sized to cover only 1 km in the height direction). Four km translates into 4x68.5 =274 arc seconds. The central spot of the Airy disk defined using eq.(29) has an angular diameter = 29.6 arc seconds at λ = 10 μ (and so has diameters of 51.5 and 18.3 arc seconds respectively at 17.4μ (mid-channel 1) and 6.2μ (mid-channel 21)). Excluding elements within +- 2 km from contributing to the integral means excluding regions which cover the peak and several of the first few dark-rings in the Airy pattern.

Note that if the atmospheric radiance profile is as shown in figure 13 (a more representative case), there will be a larger range of detector heights Δ for which $\Delta - \Delta_j = 0$ and the integral becomes more complicated since B_a now depends on Δ for $\Delta > \Delta_a$, the limit of the flat-topped region of the radiance profile.

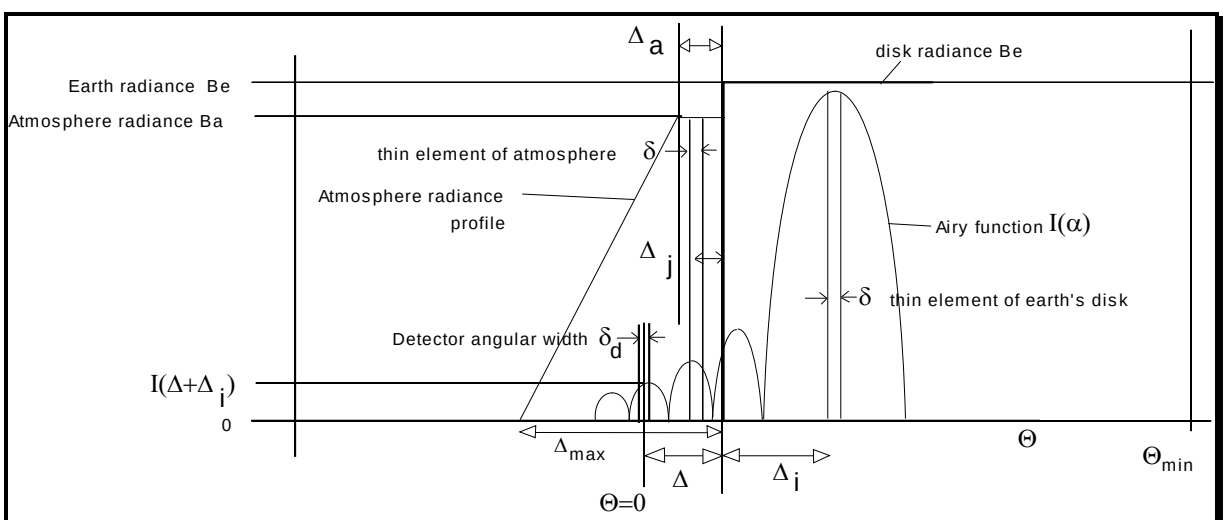

Figure 13 Trapezoidal atmospheric radiance profile case

It is obvious from eq.(48) that, in order to estimate the diffraction (or indeed the surface-scatter) contribution to the measurement of the atmospheric radiance at height Δ when the latter has a height behaviour of either of the forms shown in figs 12 and 13, we need to know the atmospheric radiance B_a and its profile. Thus we need to know that which is unknown at the start of the measurement in order to estimate the errors that diffraction (or scatter) of radiation from neighbouring atmospheric (and earth) elements are likely to contribute to the measurement of the unknown quantity.

This chicken-and-egg situation is alleviated by utilising the fiducial radiance profiles given in appendix B as a guide to the likely radiance profiles which will occur in practice. These (or approximations to them) can be used in integrals of the form given in eq.(48). However, the fact remains that there will exist unwanted contributions to the detector signal which will depend on the atmospheric radiances at distances from the instantaneous detector location in the atmosphere. This component of the background probably cannot be calibrated out and so becomes a major concern.

As an example, consider the case where $B_a = B_e$ and the radiance profile is as given in figure 12. Here, the diffractive contribution for heights beyond Δ_a can be obtained from the Table 12 values by just decrementing the Δ - values by the amount Δ_a and by using the tabulated I_{diff} values. Thus if, on a linear plot, the atmospheric radiance is flat for the first 10 km (cf figs B1, B17-B20) and drops rapidly as the height increases beyond this, table 10 values can be used for Δ>10 km by subtracting 10 km from the Δ-values given in the table and then using the scatter fractions in that table at the 'new' Δ-values. More interestingly, if $B_a \neq B_e$, then an applicable set of I_{diff} values can be computed using

$$I_{diff}(\Delta_{new}) = \frac{B_a}{B_e}\left[I_{diff}(\Delta_{new} - \Delta_a) + \left(\frac{B_e - B_a}{B_a}\right) I_{diff}(\Delta_{new}) \right] \quad (49)$$

Equation (49) reduces to

$$I_{diff}(\Delta_{new}) = I_{diff}(\Delta_{new} - \Delta_a) \quad (50)$$

if $B_a = B_e$, as noted above. It is to be understood that in order to compute actual radiances from I_{diff} values, the latter must then be multiplied by B_e (and not by B_a). It can be shown that eq.s (49) and (50) also apply when $\Delta_{new} < \Delta_a$.

To show how atmospheric emission might alter things, consider the channel 1 atmospheric radiance profile given in table B1. Here it is approximated as being constant at B_a = 2.21 watt/m^2/sr (see table 2, column 2) for the first 10 km and zero from 10 km upwards (it drops rapidly from 10 km). Taking $B_\alpha(300)$ = 3.76 watt/m^2/sr (see table 3, col5) for B_e, then eq.(49) used with the table 12 values as starting-values and (B_e- B_a)/ B_a = 0.41, B_a/ B_e = 0.59, gives the 'new' values in table 14 (the 'old' table 12 values are included for comparison). The % change due to the atmosphere is given in the last column.

Table 14 Effect of Atmospheric Radiance on Diffractive scatter estimates (channel 1)

LOS		OLD (table 12)	'shifted' OLD	NEW	% CHANGE
Δ (km)	Δ - 10(km)	$I_{diff}(\Delta)$	$I_{diff}(\Delta\text{-}10)$	$I_{diff}(\Delta)$	$\frac{100*(NEW-OLD)}{OLD}$
-20.0	-30.0	2.147*10^-2	?	-	-
-15.0	-35.0	2.146*10^-2	?	-	-
-10.0	-20.0	2.143*10^-2	2.147*10^-2	214.54*10^-4	0.11
-5.0	-15.0	2.118*10^-2	2.146*10^-2	213.45*10^-4	0.78
.0	-10.0	1.694*10^-2	2.143*10^-2	195.89*10^-4	15.64
5.0	-5.0	2.043*10^-3	2.118*10^-2	133.34*10^-4	552.67
10.0	.0	1.106*10^-3	1.694*10^-2	104.48*10^-4	844.67
15.0	5.0	7.515*10^-4	2.043*10^-3	15.13*10^-4	101.33
20.0	10.0	5.678*10^-4	1.106*10^-3	8.85*10^-4	55.86
25.0	15.0	4.609*10^-4	7.515*10^-4	6.32*10^-4	37.12
30.0	20.0	3.876*10^-4	5.678*10^-4	4.94*10^-4	27.45
35.0	25.0	3.340*10^-4	4.609*10^-4	4.09*10^-4	22.46
40.0	30.0	2.949*10^-4	3.876*10^-4	3.50*10^-4	18.68
45.0	35.0	2.641*10^-4	3.340*10^-4	3.05*10^-4	15.49
50.0	40.0	2.389*10^-4	2.949*10^-4	2.72*10^-4	13.86
55.0	45.0	2.188*10^-4	2.641*10^-4	2.46*10^-4	12.43
60.0	50.0	2.020*10^-4	2.389*10^-4	2.24*10^-4	10.89
65.0	55.0	1.874*10^-4	2.188*10^-4	2.06*10^-4	9.93
70.0	60.0	1.752*10^-4	2.020*10^-4	1.91*10^-4	9.02
75.0	65.0	1.646*10^-4	1.874*10^-4	1.78*10^-4	8.14
80.0	70.0	1.552*10^-4	1.752*10^-4	1.67*10^-4	7.60
85.0	75.0	1.469*10^-4	1.646*10^-4	1.57*10^-4	6.88
90.0	80.0	1.397*10^-4	1.552*10^-4	1.49*10^-4	6.66
95.0	85.0	1.331*10^-4	1.469*10^-4	1.41*10^-4	5.94
100.0	90.0	1.272*10^-4	1.397*10^-4	1.35*10^-4	6.13

Table 14 shows large %-age changes in the diffractive scatter fractions at around LOS height 10 km, which marks a transition boundary in the atmospheric radiance height profile assumed for channel 1. This means that estimates of the diffractive scatter fractions will be quite inaccurate in these regions if atmospheric radiance is neglected. The table shows that, whereas a diffractive scatter fraction of 0.11 % of the disk radiance is indicated at LOS = 10 km **before** atmospheric radiance effects are included, the diffractive scatter fraction can be 1.04 % (10 times bigger) at the same LOS height **after** atmospheric radiance effects are included. This large change to an unwanted scattered background whose magnitude is subject to details of the unknown atmospheric radiance profile creates a large uncertainty in its value. This results in a correspondingly large uncertainty in how much of the scattered background budget this component will cover.

As a contrast, table 15 shows the effect of the same assumed atmospheric radiance profile on the incoherent (mirror) scatter fractions. The scatter fractions were taken from table 10 (col.4). The % changes in the scatter fractions are seen to be negligible in this case. The reason for the different behaviour is the much slower variation with LOS height near a transition boundary of the incoherent scatter component compared with the variation that the diffractive component undergoes.

Table 15 Effect of Atmospheric Radiance on Incoherent (mirror) scatter estimates (channel 1)

LOS		OLD(table 10)	'shifted' OLD	NEW	PERCENT CHANGE
Δ (km)	Δ - 10(km)	$I_{diff}(\Delta)$	$I_{diff}(\Delta-10)$	$I_{diff}(\Delta)$	100*(NEW-OLD)/OLD
-20.0	-30.0	11.39*10^-5	?		
-15.0	-35.0	11.27*10^-5	?		
-10.0	-20.0	11.13*10^-5	11.39*10^-5	1.13*10^-4	1.53
-5.0	-15.0	10.92*10^-5	11.27*10^-5	1.11*10^-4	1.65
.0	-10.0	10.69*10^-5	11.13*10^-5	1.09*10^-4	1.96
5.0	-5.0	10.18*10^-5	10.92*10^-5	1.06*10^-4	4.13
10.0	.0	9.98*10^-5	10.69*10^-5	1.04*10^-4	4.21
15.0	5.0	9.83*10^-5	10.18*10^-5	1.00*10^-4	1.73
20.0	10.0	9.71*10^-5	9.98*10^-5	0.99*10^-4	1.96
25.0	15.0	9.62*10^-5	9.83*10^-5	0.97*10^-4	0.83
30.0	20.0	9.53*10^-5	9.71*10^-5	0.96*10^-4	0.73
35.0	25.0	9.45*10^-5	9.62*10^-5	0.96*10^-4	1.59
40.0	30.0	9.38*10^-5	9.53*10^-5	0.95*10^-4	1.28
45.0	35.0	9.31*10^-5	9.45*10^-5	0.94*10^-4	0.97
50.0	40.0	9.25*10^-5	9.38*10^-5	0.93*10^-4	0.54
55.0	45.0	9.19*10^-5	9.31*10^-5	0.93*10^-4	1.20
60.0	50.0	9.13*10^-5	9.25*10^-5	0.92*10^-4	0.77
65.0	55.0	9.08*10^-5	9.19*10^-5	0.91*10^-4	0.22
70.0	60.0	9.03*10^-5	9.13*10^-5	0.91*10^-4	0.78
75.0	65.0	8.98*10^-5	9.08*10^-5	0.90*10^-4	0.22
80.0	70.0	8.94*10^-5	9.03*10^-5	0.90*10^-4	0.67
85.0	75.0	8.89*10^-5	8.98*10^-5	0.89*10^-4	0.11
90.0	80.0	8.85*10^-5	8.94*10^-5	0.89*10^-4	0.56
95.0	85.0	8.81*10^-5	8.89*10^-5	0.89*10^-4	1.02
100.0	90.0	8.77*10^-5	8.85*10^-5	0.88*10^-4	0.34

13.0 Comparison of expected scatter radiances and background budget values

Table 13 shows that the diffractive scatter fraction (to be multiplied by an assumed value for B_α , the in-band earth's disk radiance, to get scatter radiance) is generally several times bigger than the corresponding incoherent mirror scatter fraction for the same height, at all LOS heights. It must therefore be regarded as the dominant source of scattered background in the absence of a component used to diminish it (e.g. a Lyot stop). Note that the table 12 estimates of the diffractive scatter are to be taken as **per fully- illuminated aperture**, so they must be multiplied by the number of mirror apertures that are directly illuminated by earth radiance. It will be reduced if any aperture contributing diffraction is partially-illuminated, by roughly that fraction of the aperture which is illuminated.

Table 14 shows that there could be a large uncertainty in the diffractive scatter component, depending on the accuracy with which the actual atmospheric radiance profile is known. In what follows, diffractive scatter estimates will first of all be based on assuming zero effect due to the atmosphere. Because at least two mirrors (the scan and the primary) will be illuminated by unattenuated earth radiance, a factor of two will be included into the diffractive scatter estimates.

13.1 Background Budgets

Perusal of the HIRDLS IRD and ITS yields the following specification for the levels that out-of-fov scatter must satisfy:

less than 1% of the total signal radiance in the detector fov, or
less than that portion of the signal radiance equivalent to 1/4 of a NEN , whichever is the larger,
shall originate from regions more than 2.5 km above and below the detector centre-line.

This is taken to mean that, where the atmospheric radiance signal is larger than 100x1/4xNEN, the background signal must be less than 1% of the atmospheric radiance signal and where the atmospheric radiance signal is less than 100x1/4xNEN, the background signal must be less than 1/4 NEN.

In order to make most use of the atmospheric radiance profiles given in tables B1-B21, the LH scale of each plot has been modified to indicate a scale shifted up by a factor 100 relative to the RH scale. Thus if one uses the RH scale, one can read off atmospheric radiance against LOS height, whereas if one uses the modified LH scale, one can read off 1/100th of the

atmospheric radiance against LOS height. In this way, the profile drawn can be also used to see where a radiance equal to 1 % of the atmospheric radiance falls at each height. If horizontal lines at 0.25 NEN are marked for each vertical scale, one can immediately see when the atmospheric signal has dropped to 0.25 NEN and when 1% of it has dropped to 0.25 NEN. The LOS height at which the latter occurs marks the point (to be referred to as the 'cross-over' height) at which the scatter budget switches from using the 1% signal level to using the 0.25 NEN level as the driver.

13.2 Diffractive scatter compared with budgets

Tables 16A, 16B and 16C show diffractive scatter estimates as a function of LOS height, based on table 13 values for I_{diff} multiplied by the appropriate $B_\alpha(300)$ value for the channel taken from table 3, scaled for two illuminated apertures and linearly scaled with the central wavelength of the pass band for each channel. Some of these values are plotted using the LH scale of figures B1-B21. They are plotted using the symbol -⊕- . This allows one to immediately see if the 1% of the atmosphere signal level exceeds the diffractive scatter or not.

Table 16A Diffractive scatter estimates - channels 1 - 7

	DIFFRACTIVE SCATTER CONTRIBUTIONS watt/m2/sr			Idiff (table 13) scaled from 10μ to each wavelength λ + scaled for 2 apertures + scaled by $B_\alpha(300)$ (table 1, col 7)			
Channel α→	1	2	3	4	5	6	7
$B_\alpha(300)$ →	3.76	2.49	4.63	4.99	3.77	1.95	2.37
(λ)→	17.38	16.47	16.00	15.56	14.99	12.07	11.85
Δ(km)							
.0	2214.02*10^-4	1389.43*10^-4	2509.83*10^-4	2630.59*10^-4	1914.64*10^-4	797.42*10^-4	951.50*10^-4
5.0	267.02*10^-4	167.57*10^-4	302.69*10^-4	317.26*10^-4	230.91*10^-4	96.17*10^-4	114.75*10^-4
10.0	144.55*10^-4	90.71*10^-4	163.86*10^-4	171.75*10^-4	125.01*10^-4	52.06*10^-4	62.12*10^-4
20.0	74.21*10^-4	46.57*10^-4	84.13*10^-4	88.17*10^-4	64.18*10^-4	26.73*10^-4	31.89*10^-4
30.0	50.66*10^-4	31.79*10^-4	57.43*10^-4	60.19*10^-4	43.81*10^-4	18.25*10^-4	21.77*10^-4
40.0	38.54*10^-4	24.19*10^-4	43.69*10^-4	45.79*10^-4	33.33*10^-4	13.88*10^-4	16.56*10^-4
50.0	31.22*10^-4	19.59*10^-4	35.40*10^-4	37.10*10^-4	27.00*10^-4	11.25*10^-4	13.42*10^-4
60.0	26.40*10^-4	16.57*10^-4	29.93*10^-4	31.37*10^-4	22.83*10^-4	9.51*10^-4	11.35*10^-4
70.0	22.90*10^-4	14.37*10^-4	25.96*10^-4	27.21*10^-4	19.80*10^-4	8.25*10^-4	9.84*10^-4
80.0	20.28*10^-4	12.73*10^-4	22.99*10^-4	24.10*10^-4	17.54*10^-4	7.31*10^-4	8.72*10^-4
90.0	18.26*10^-4	11.46*10^-4	20.70*10^-4	21.69*10^-4	15.79*10^-4	6.58*10^-4	7.85*10^-4
100.0	16.62*10^-4	10.43*10^-4	18.85*10^-4	19.75*10^-4	14.38*10^-4	5.99*10^-4	7.14*10^-4

Table 16B Diffractive scatter estimates - channels 8-14

	DIFFRACTIVE SCATTER CONTRIBUTIONS watt/m2/sr			Idiff (table 13) scaled from 10μ to each wavelength λ + scaled for 2 apertures + scaled by $B_\alpha(300)$ (table 1, col 7)			
Channel α→	8	9	10	11	12	13	14
$B_\alpha(300)$ →	5.42	2.01	1.97	4.47	1.57	1.22	1.83
(λ)→	11.34	10.82	10.05	9.58	8.85	8.26	8.04
Δ(km)							
.0	2082.36*10^-4	736.83*10^-4	670.77*10^-4	1450.83*10^-4	470.75*10^-4	341.42*10^-4	498.48*10^-4
5.0	251.14*10^-4	88.86*10^-4	80.90*10^-4	174.97*10^-4	56.77*10^-4	41.18*10^-4	60.12*10^-4
10.0	135.96*10^-4	48.11*10^-4	43.79*10^-4	94.72*10^-4	30.73*10^-4	22.29*10^-4	32.55*10^-4
20.0	69.80*10^-4	24.70*10^-4	22.48*10^-4	48.63*10^-4	15.78*10^-4	11.44*10^-4	16.71*10^-4
30.0	47.65*10^-4	16.86*10^-4	15.35*10^-4	33.20*10^-4	10.77*10^-4	7.81*10^-4	11.41*10^-4
40.0	36.25*10^-4	12.83*10^-4	11.68*10^-4	25.26*10^-4	8.19*10^-4	5.94*10^-4	8.68*10^-4
50.0	29.37*10^-4	10.39*10^-4	9.46*10^-4	20.46*10^-4	6.64*10^-4	4.81*10^-4	7.03*10^-4
60.0	24.83*10^-4	8.79*10^-4	8.00*10^-4	17.30*10^-4	5.61*10^-4	4.07*10^-4	5.94*10^-4
70.0	21.54*10^-4	7.62*10^-4	6.94*10^-4	15.01*10^-4	4.87*10^-4	3.53*10^-4	5.16*10^-4
80.0	19.08*10^-4	6.75*10^-4	6.15*10^-4	13.29*10^-4	4.31*10^-4	3.13*10^-4	4.57*10^-4
90.0	17.17*10^-4	6.08*10^-4	5.53*10^-4	11.96*10^-4	3.88*10^-4	2.82*10^-4	4.11*10^-4
100.0	15.64*10^-4	5.53*10^-4	5.04*10^-4	10.89*10^-4	3.53*10^-4	2.56*10^-4	3.74*10^-4

Table 16C Diffractive scatter estimates - channels 15 - 21

	DIFFRACTIVE SCATTER CONTRIBUTIONS watt/m2/sr			Idiff (table 13) scaled from 10μ to each wavelength λ + scaled for 2 apertures + scaled by $B_\alpha(300)$ (table 1, col 7)			
Channel α→	15	16	17	18	19	20	21
$B_\alpha(300)$ →	1.38	1.04	2.12	1.87	0.52	3.85	1.12
(λ)→	7.88	7.76	7.42	7.09	0.00	0.00	0.00
Δ(km)							
.0	368.42*10^-4	273.43*10^-4	532.95*10^-4	449.19*10^-4	17.62*10^-4	130.44*10^-4	37.95*10^-4
5.0	44.43*10^-4	32.98*10^-4	64.27*10^-4	54.17*10^-4	2.12*10^-4	15.73*10^-4	4.58*10^-4
10.0	24.05*10^-4	17.85*10^-4	34.80*10^-4	29.33*10^-4	1.15*10^-4	8.52*10^-4	2.48*10^-4
20.0	12.35*10^-4	9.16*10^-4	17.86*10^-4	15.06*10^-4	0.59*10^-4	4.37*10^-4	1.27*10^-4
30.0	8.43*10^-4	6.26*10^-4	12.19*10^-4	10.28*10^-4	0.40*10^-4	2.98*10^-4	0.87*10^-4
40.0	6.41*10^-4	4.76*10^-4	9.28*10^-4	7.82*10^-4	0.31*10^-4	2.27*10^-4	0.66*10^-4
50.0	5.20*10^-4	3.86*10^-4	7.52*10^-4	6.33*10^-4	0.25*10^-4	1.84*10^-4	0.54*10^-4
60.0	4.39*10^-4	3.26*10^-4	6.36*10^-4	5.36*10^-4	0.21*10^-4	1.56*10^-4	0.45*10^-4
70.0	3.81*10^-4	2.83*10^-4	5.51*10^-4	4.65*10^-4	0.18*10^-4	1.35*10^-4	0.39*10^-4
80.0	3.38*10^-4	2.51*10^-4	4.88*10^-4	4.12*10^-4	0.16*10^-4	1.20*10^-4	0.35*10^-4
90.0	3.04*10^-4	2.25*10^-4	4.40*10^-4	3.70*10^-4	0.15*10^-4	1.08*10^-4	0.31*10^-4
100.0	2.77*10^-4	2.05*10^-4	4.00*10^-4	3.37*10^-4	0.13*10^-4	0.98*10^-4	0.28*10^-4

The figures show that the diffractive scatter curves generally remain above the 1% signal level curve and are all well above the 0.25 NEN level at 80 km in all but the 3 shortest-wavelength channels 19-21. Figure B19 shows that only in channel 19 does the diffracted scatter curve fall below the 0.25 NEN line (from about 20km upwards to 80 km). This behaviour follows from the diffractive scatter being linearly proportional to wavelength λ.

13.3 Incoherent (surface) scatter compared with budgets

Tables 17A, 17B and 17C show surface scatter estimates as a function of LOS height, based on table 13 values for I_{scat} multiplied by the appropriate Bα(300) value for the channel taken from table 3, scaled to the central wavelength of the pass band for each channel using the scale factors in table 7. Some of these values are plotted using the LH scale of figures B1-B21. They are plotted using the symbol -×- .This allows one to immediately see if the 1% of the atmosphere signal level exceeds the surface scatter or not.

The figures show that the incoherent scatter curves for the longer wavelength channels (1 and 2) fall below the 0.25 NEN level from 0 km to 80 km, but that the curves for all other channels are all above the 0.25 NEN line. As the channel wavelength decreases (increasing channel number) the scatter levels rise as one would expect, given the $1/\lambda^2$ behaviour assumed for the incoherent surface scatter.

Table 17A Surface scatter estimates - channels 1 - 7

	SURFACE SCATTER CONTRIBUTIONS watt/m2/sr			Iscat (table 13) scaled from 10μ to each wavelength λ + scaled by $B_\alpha(300)$ (table 1, col 7)			
Channel α→	1	2	3	4	5	6	7
$B_\alpha(300)$ →	3.76	2.49	4.63	4.99	3.77	1.95	2.37
(λ)→	17.38	16.47	16.00	15.56	14.99	12.07	11.85
Δ(km)							
.0	14.87*10^-5	10.91*10^-5	21.78*10^-5	24.54*10^-5	20.15*10^-5	16.05*10^-5	20.27*10^-5
5.0	14.16*10^-5	10.39*10^-5	20.74*10^-5	23.37*10^-5	19.19*10^-5	15.29*10^-5	19.30*10^-5
10.0	13.88*10^-5	10.19*10^-5	20.33*10^-5	22.91*10^-5	18.81*10^-5	14.98*10^-5	18.92*10^-5
20.0	13.51*10^-5	9.91*10^-5	19.78*10^-5	22.29*10^-5	18.30*10^-5	14.58*10^-5	18.41*10^-5
30.0	13.26*10^-5	9.73*10^-5	19.41*10^-5	21.88*10^-5	17.96*10^-5	14.31*10^-5	18.07*10^-5
40.0	13.05*10^-5	9.58*10^-5	19.11*10^-5	21.53*10^-5	17.68*10^-5	14.08*10^-5	17.78*10^-5
50.0	12.87*10^-5	9.44*10^-5	18.84*10^-5	21.23*10^-5	17.44*10^-5	13.89*10^-5	17.54*10^-5
60.0	12.70*10^-5	9.32*10^-5	18.60*10^-5	20.96*10^-5	17.21*10^-5	13.71*10^-5	17.31*10^-5
70.0	12.56*10^-5	9.22*10^-5	18.40*10^-5	20.73*10^-5	17.02*10^-5	13.56*10^-5	17.12*10^-5
80.0	12.44*10^-5	9.13*10^-5	18.21*10^-5	20.52*10^-5	16.85*10^-5	13.42*10^-5	16.95*10^-5
90.0	12.31*10^-5	9.03*10^-5	18.03*10^-5	20.31*10^-5	16.68*10^-5	13.29*10^-5	16.78*10^-5
100.0	12.20*10^-5	8.95*10^-5	17.87*10^-5	20.13*10^-5	16.53*10^-5	13.17*10^-5	16.63*10^-5

Table 17B Surface scatter estimates - channels 8-14

	SURFACE SCATTER CONTRIBUTIONS watt/m2/sr			Iscat (table 13) scaled from 10μ to each wavelength λ + scaled by $B_\alpha(300)$ (table 1, col 7)			
Channel α→	8	9	10	11	12	13	14
$B_\alpha(300)$ →	5.42	2.01	1.97	4.47	1.57	1.22	1.83
(λ)→	11.34	10.82	10.05	9.58	8.85	0.00	8.04
Δ(km)							
.0	50.41*10^-5	20.63*10^-5	23.38*10^-5	58.30*10^-5	24.00*10^-5	21.52*10^-5	34.04*10^-5
5.0	48.00*10^-5	19.64*10^-5	22.26*10^-5	55.52*10^-5	22.86*10^-5	20.49*10^-5	32.42*10^-5
10.0	47.06*10^-5	19.26*10^-5	21.82*10^-5	54.42*10^-5	22.41*10^-5	20.09*10^-5	31.78*10^-5
20.0	45.79*10^-5	18.74*10^-5	21.23*10^-5	52.95*10^-5	21.80*10^-5	19.55*10^-5	30.92*10^-5
30.0	44.94*10^-5	18.39*10^-5	20.84*10^-5	51.97*10^-5	21.40*10^-5	19.18*10^-5	30.35*10^-5
40.0	44.23*10^-5	18.10*10^-5	20.51*10^-5	51.15*10^-5	21.06*10^-5	18.88*10^-5	29.87*10^-5
50.0	43.62*10^-5	17.85*10^-5	20.23*10^-5	50.44*10^-5	20.77*10^-5	18.62*10^-5	29.45*10^-5
60.0	43.05*10^-5	17.62*10^-5	19.96*10^-5	49.79*10^-5	20.50*10^-5	18.38*10^-5	29.07*10^-5
70.0	42.58*10^-5	17.42*10^-5	19.75*10^-5	49.24*10^-5	20.27*10^-5	18.18*10^-5	28.75*10^-5
80.0	42.16*10^-5	17.25*10^-5	19.55*10^-5	48.75*10^-5	20.07*10^-5	18.00*10^-5	28.47*10^-5
90.0	41.73*10^-5	17.08*10^-5	19.35*10^-5	48.26*10^-5	19.87*10^-5	17.82*10^-5	28.18*10^-5
100.0	41.35*10^-5	16.92*10^-5	19.18*10^-5	47.83*10^-5	19.69*10^-5	17.65*10^-5	27.93*10^-5

Table 17C Surface scatter estimates - channels 15 - 21

	SURFACE SCATTER CONTRIBUTIONS watt/m2/sr			Iscat (table 13) scaled from 10μ to each wavelength λ + scaled by $B_\alpha(300)$ (table 1, col 7)			
Channel α→	15	16	17	18	19	20	21
$B_\alpha(300)$ →	1.38	1.04	2.12	1.87	0.52	3.85	1.12
(λ)→	7.88	7.76	7.42	7.09	0.00	0.00	0.00
Δ(km)							
.0	26.70*10^-5	20.79*10^-5	46.23*10^-5	44.78*10^-5	5.56*10^-5	41.16*10^-5	11.97*10^-5
5.0	25.43*10^-5	19.80*10^-5	44.03*10^-5	42.64*10^-5	5.29*10^-5	39.19*10^-5	11.40*10^-5
10.0	24.93*10^-5	19.41*10^-5	43.16*10^-5	41.80*10^-5	5.19*10^-5	38.42*10^-5	11.18*10^-5
20.0	24.25*10^-5	18.88*10^-5	41.99*10^-5	40.67*10^-5	5.05*10^-5	37.38*10^-5	10.88*10^-5
30.0	23.80*10^-5	18.53*10^-5	41.22*10^-5	39.92*10^-5	4.96*10^-5	36.69*10^-5	10.67*10^-5
40.0	23.43*10^-5	18.24*10^-5	40.57*10^-5	39.29*10^-5	4.88*10^-5	36.11*10^-5	10.51*10^-5
50.0	23.10*10^-5	17.99*10^-5	40.00*10^-5	38.75*10^-5	4.81*10^-5	35.61*10^-5	10.36*10^-5
60.0	22.80*10^-5	17.76*10^-5	39.49*10^-5	38.24*10^-5	4.75*10^-5	35.15*10^-5	10.23*10^-5
70.0	22.56*10^-5	17.56*10^-5	39.05*10^-5	37.82*10^-5	4.70*10^-5	34.77*10^-5	10.11*10^-5
80.0	22.33*10^-5	17.39*10^-5	38.66*10^-5	37.45*10^-5	4.65*10^-5	34.42*10^-5	10.01*10^-5
90.0	22.11*10^-5	17.21*10^-5	38.27*10^-5	37.07*10^-5	4.60*10^-5	34.07*10^-5	9.91*10^-5
100.0	21.91*10^-5	17.06*10^-5	37.93*10^-5	36.74*10^-5	4.56*10^-5	33.76*10^-5	9.82*10^-5

14.0 Conclusions from the Comparison of diffractive and incoherent scatter with budgets

It is considered a requirement that the diffractive scatter and incoherent scatter curves shown in figures B1 - B21 should **individually** fall below the composite curve (henceforth called 'the budget curve') formed by the 1% signal level and the 0.25 NEN level (the latter taking over when it is the larger of the two). Eventually, it must be the aim that the **sum** of the diffractive and the incoherent scatter curves should satisfy this requirement. Examination of fig. B1-B21 shows that the scatter curves must be multiplied by various fractional factors in order to bring their levels below the budget curve. These factors are estimated here.

Because of the shapes of the various curves, it appears likely that, if a scatter curve can be brought below the budget curve at the point where the 1% signal curve and the 0.25 NEN line intersect, the scatter curve will fall below the budget curve at all heights. So it is the factor by which a scatter curve exceeds the budget curve at the height-value where this cross-over occurs which is the important factor. The following table lists the cross-over heights in each channel and the estimated factor (scatter curve value/budget curve value) at these heights for each scatter contribution (diffractive and surface).

Table 18 Scatter signal excess factors over 0.25 NEN levels at the cross-over height

Channel α	λ mean (μ)	$B_e(300)$ Earth + structure Blackbody in-band radiance (watt/m2/sr)	0.25 NEN_α radiance (watt/m2/sr)	cross-over signal 100x0.25 NEN_α (watt/m2/sr)	approx. cross-over height (km)	S_{diff} diffractive scatter radiance at cross-over height (watt/m2/sr)	S_{diff}/0.25 NEN Diffractive scatter excess factor	S_{scat} surface scatter radiance at cross-over height (watt/m2/sr)	S_{scat}/0.25 NEN surface scatter excess factor
1	17.38	3.76	30.00*10^-5	30.00*10^-3	45	34.88*10^-4	11.6	1.30*10^-4	0.4
2	16.47	2.49	15.75*10^-5	15.75*10^-3	55	18.08*10^-4	11.5	0.94*10^-4	0.6
3	16.00	4.63	14.75*10^-5	14.75*10^-3	66	27.55*10^-4	18.7	1.85*10^-4	1.3
4	15.56	4.99	15.00*10^-5	15.00*10^-3	71	26.90*10^-4	17.9	2.07*10^-4	1.4
5	14.99	3.77	10.75*10^-5	10.75*10^-3	77	18.22*10^-4	16.9	1.69*10^-4	1.6
6	12.07	1.95	4.75*10^-5	4.75*10^-3	22	25.03*10^-4	52.7	1.45*10^-4	3.1
7	11.85	2.37	5.00*10^-5	5.00*10^-3	25	26.83*10^-4	53.7	1.82*10^-4	3.6
8	11.34	5.42	5.25*10^-5	5.25*10^-3	38	38.53*10^-4	73.4	4.44*10^-4	8.5
9	10.82	2.01	5.00*10^-5	5.00*10^-3	29	17.64*10^-4	35.3	1.84*10^-4	3.7
10	10.05	1.97	3.75*10^-5	3.75*10^-3	61	7.89*10^-4	21.0	2.05*10^-4	5.5
11	9.58	4.47	6.00*10^-5	6.00*10^-3	68	15.47*10^-4	25.8	4.93*10^-4	8.2
12	8.85	1.57	2.50*10^-5	2.50*10^-3	56	6.02*10^-4	24.1	2.06*10^-4	8.2
13	8.26	1.22	2.75*10^-5	2.75*10^-3	39	6.13*10^-4	22.3	1.89*10^-4	6.9
14	8.04	1.83	2.75*10^-5	2.75*10^-3	45	7.85*10^-4	28.5	2.97*10^-4	10.8
15	7.88	1.38	2.75*10^-5	2.75*10^-3	47	5.56*10^-4	20.2	2.32*10^-4	8.4
16	7.76	1.04	2.75*10^-5	2.75*10^-3	46	4.22*10^-4	15.3	1.81*10^-4	6.6
17	7.42	2.12	3.00*10^-5	3.00*10^-3	49	7.70*10^-4	25.7	4.01*10^-4	13.4
18	7.09	1.87	3.00*10^-5	3.00*10^-3	48	6.63*10^-4	22.1	3.89*10^-4	13.0
19	7.10	0.52	3.25*10^-5	3.25*10^-3	23	0.53*10^-4	1.6	0.50*10^-4	1.5
20	6.76	3.85	4.00*10^-5	4.00*10^-3	53	1.76*10^-4	4.4	3.55*10^-4	8.9
21	6.22	1.12	2.75*10^-5	2.75*10^-3	45	0.60*10^-4	2.2	1.04*10^-4	3.8

The table shows that diffractive scatter excesses range from a factor 1.6 (in channel 19, λ = 7.1 μ) to as much as a factor 74 (in channel 8, λ = 11.34 μ) over the 0.25 NEN level at the cross-over height. The largest surface scatter excess factor is about 13 (in channel 17, λ = 7.42 μ). Note that the scatter radiances are critically dependant on the value used for the emissivity $\boldsymbol{\varepsilon}$ of the earth (and structure) in each channel. The above figures were computed assuming the worst case value $\boldsymbol{\varepsilon = 1}$. An emissivity value < 1 will cause directly reduced scatter estimates and directly reduced scatter excess factors. On the other hand, if the diffractive and surface scatter can only be allotted a fraction of a 0.25 NEN budget, the excess factors for each will increase in inverse proportion to the size of this fraction of the budget allotted to them.

If the whole of the mirror surface scatter signal can be calibrated out (because of its predicted weak variation with LOS height), then it need not be allotted a portion of the background budget and the whole of it can be given to the diffractive scatter (only a small part of which might be calibrated out). If this is the case, then in order to achieve reduction of the uncalibrated diffractive scattered background down to the budget level of 0.25 NEN in all channels, the diffractive scatter must be reduced by at least a factor of 75 below the presently predicted levels. A reduction by a factor 30 would reduce diffractive scatter to 0.25 NEN levels in all except 4 channels (6 → 9).

The final conclusion is that, unless the diffractive scatter estimates for channel 8 are too high by a factor about 100, one or more Lyot stops are required in the HIRDLS optical system in order to permit interception and attenuation of diffractive scatter from one or more earthlight-illuminated apertures. This conclusion poses difficult questions for the present design as to where such stops might be located and concerning where to locate the system aperture stop.

Appendix A: Tables 8, 9 and 11

Tables 8A - 8I Surface scatter fractions

Table 8A Θ_{min} = 5.0 deg , Θ_{max} = 90.00 deg

	Θ_{min} = 5.0 deg	INTEGRALS	Θ_{max} = 90.0 deg
Δ (km)	$I_{earth}(\Theta<\Theta_{min},\Delta)$	$I_{struc}(\Theta_{min},\Theta_{max})$	$I_{earth}+I_{struc}$,
-20.0	1.788*10^-5	6.953*10^-5	8.741*10^-5
-15.0	1.718*10^-5	6.953*10^-5	8.671*10^-5
-10.0	1.629*10^-5	6.953*10^-5	8.582*10^-5
-5.0	1.498*10^-5	6.953*10^-5	8.451*10^-5
.0	1.360*10^-5	6.953*10^-5	8.313*10^-5
5.0	1.028*10^-5	6.953*10^-5	7.981*10^-5
10.0	9.019*10^-6	6.953*10^-5	7.855*10^-5
15.0	8.145*10^-6	6.953*10^-5	7.767*10^-5
20.0	7.461*10^-6	6.953*10^-5	7.699*10^-5
25.0	6.892*10^-6	6.953*10^-5	7.642*10^-5
30.0	6.404*10^-6	6.953*10^-5	7.593*10^-5
35.0	5.974*10^-6	6.953*10^-5	7.550*10^-5
40.0	5.589*10^-6	6.953*10^-5	7.512*10^-5
45.0	5.240*10^-6	6.953*10^-5	7.477*10^-5
50.0	4.921*10^-6	6.953*10^-5	7.445*10^-5
55.0	4.626*10^-6	6.953*10^-5	7.416*10^-5
60.0	4.353*10^-6	6.953*10^-5	7.388*10^-5
65.0	4.099*10^-6	6.953*10^-5	7.363*10^-5
70.0	3.860*10^-6	6.953*10^-5	7.339*10^-5
75.0	3.636*10^-6	6.953*10^-5	7.317*10^-5
80.0	3.425*10^-6	6.953*10^-5	7.295*10^-5
85.0	3.225*10^-6	6.953*10^-5	7.275*10^-5
90.0	3.036*10^-6	6.953*10^-5	7.257*10^-5
95.0	2.856*10^-6	6.953*10^-5	7.239*10^-5
100.0	2.685*10^-6	6.953*10^-5	7.222*10^-5

Table 8B Θ_{min} = 10.0 deg , Θ_{max} = 90.00 deg

	Θ_{min} = 10.0 deg	INTEGRALS	Θ_{max} = 90.0 deg
Δ (km)	$I_{earth}(\Theta<\Theta_{min},\Delta)$	$I_{struc}(\Theta_{min},\Theta_{max})$	$I_{earth}+I_{struc}$,
-20.0	2.433*10^-5	5.706*10^-5	8.139*10^-5
-15.0	2.359*10^-5	5.706*10^-5	8.065*10^-5
-10.0	2.264*10^-5	5.706*10^-5	7.970*10^-5
-5.0	2.128*10^-5	5.706*10^-5	7.834*10^-5
.0	1.984*10^-5	5.706*10^-5	7.690*10^-5
5.0	1.647*10^-5	5.706*10^-5	7.353*10^-5
10.0	1.515*10^-5	5.706*10^-5	7.221*10^-5
15.0	1.423*10^-5	5.706*10^-5	7.129*10^-5
20.0	1.349*10^-5	5.706*10^-5	7.055*10^-5
25.0	1.287*10^-5	5.706*10^-5	6.993*10^-5
30.0	1.233*10^-5	5.706*10^-5	6.939*10^-5
35.0	1.184*10^-5	5.706*10^-5	6.890*10^-5
40.0	1.140*10^-5	5.706*10^-5	6.846*10^-5
45.0	1.100*10^-5	5.706*10^-5	6.806*10^-5
50.0	1.063*10^-5	5.706*10^-5	6.769*10^-5
55.0	1.028*10^-5	5.706*10^-5	6.734*10^-5
60.0	9.953*10^-6	5.706*10^-5	6.701*10^-5
65.0	9.644*10^-6	5.706*10^-5	6.670*10^-5
70.0	9.352*10^-6	5.706*10^-5	6.641*10^-5
75.0	9.073*10^-6	5.706*10^-5	6.613*10^-5
80.0	8.808*10^-6	5.706*10^-5	6.587*10^-5
85.0	8.553*10^-6	5.706*10^-5	6.561*10^-5
90.0	8.309*10^-6	5.706*10^-5	6.537*10^-5
95.0	8.074*10^-6	5.706*10^-5	6.513*10^-5
100.0	7.848*10^-6	5.706*10^-5	6.491*10^-5

Table 8C Θ_{min} = 15.0 deg , Θ_{max} = 90.00 deg

	Θ_{min} = 15.0 deg	**INTEGRALS**	Θ_{max} = 90.0 deg
Δ (km)	$I_{earth}(\Theta<\Theta_{min},\Delta)$	$I_{struc}(\Theta_{min},\Theta_{max})$	$I_{earth}+I_{struc}$,
-20.0	3.001*10^-5	4.594*10^-5	7.595*10^-5
-15.0	2.923*10^-5	4.594*10^-5	7.517*10^-5
-10.0	2.826*10^-5	4.594*10^-5	7.420*10^-5
-5.0	2.687*10^-5	4.594*10^-5	7.281*10^-5
.0	2.540*10^-5	4.594*10^-5	7.134*10^-5
5.0	2.201*10^-5	4.594*10^-5	6.794*10^-5
10.0	2.066*10^-5	4.594*10^-5	6.660*10^-5
15.0	1.971*10^-5	4.594*10^-5	6.565*10^-5
20.0	1.894*10^-5	4.594*10^-5	6.488*10^-5
25.0	1.830*10^-5	4.594*10^-5	6.423*10^-5
30.0	1.773*10^-5	4.594*10^-5	6.366*10^-5
35.0	1.722*10^-5	4.594*10^-5	6.315*10^-5
40.0	1.675*10^-5	4.594*10^-5	6.269*10^-5
45.0	1.632*10^-5	4.594*10^-5	6.226*10^-5
50.0	1.592*10^-5	4.594*10^-5	6.186*10^-5
55.0	1.554*10^-5	4.594*10^-5	6.148*10^-5
60.0	1.519*10^-5	4.594*10^-5	6.113*10^-5
65.0	1.485*10^-5	4.594*10^-5	6.079*10^-5
70.0	1.453*10^-5	4.594*10^-5	6.047*10^-5
75.0	1.423*10^-5	4.594*10^-5	6.016*10^-5
80.0	1.393*10^-5	4.594*10^-5	5.987*10^-5
85.0	1.365*10^-5	4.594*10^-5	5.959*10^-5
90.0	1.338*10^-5	4.594*10^-5	5.932*10^-5
95.0	1.311*10^-5	4.594*10^-5	5.905*10^-5
100.0	1.286*10^-5	4.594*10^-5	5.880*10^-5

Table 8D Θ_{min} = 20.0 deg , Θ_{max} = 90.00 deg

	Θ_{min} = 20.0 deg	**INTEGRALS**	Θ_{max} = 90.0 deg
Δ (km)	$I_{earth}(\Theta<\Theta_{min},\Delta)$	$I_{struc}(\Theta_{min},\Theta_{max})$	$I_{earth}+I_{struc}$,
-20.0	3.496*10^-5	3.617*10^-5	7.114*10^-5
-15.0	3.417*10^-5	3.617*10^-5	7.035*10^-5
-10.0	3.318*10^-5	3.617*10^-5	6.936*10^-5
-5.0	3.178*10^-5	3.617*10^-5	6.795*10^-5
.0	3.029*10^-5	3.617*10^-5	6.646*10^-5
5.0	2.688*10^-5	3.617*10^-5	6.305*10^-5
10.0	2.552*10^-5	3.617*10^-5	6.169*10^-5
15.0	2.455*10^-5	3.617*10^-5	6.072*10^-5
20.0	2.376*10^-5	3.617*10^-5	5.994*10^-5
25.0	2.310*10^-5	3.617*10^-5	5.927*10^-5
30.0	2.251*10^-5	3.617*10^-5	5.868*10^-5
35.0	2.198*10^-5	3.617*10^-5	5.816*10^-5
40.0	2.150*10^-5	3.617*10^-5	5.767*10^-5
45.0	2.105*10^-5	3.617*10^-5	5.723*10^-5
50.0	2.063*10^-5	3.617*10^-5	5.681*10^-5
55.0	2.024*10^-5	3.617*10^-5	5.641*10^-5
60.0	1.987*10^-5	3.617*10^-5	5.604*10^-5
65.0	1.952*10^-5	3.617*10^-5	5.569*10^-5
70.0	1.918*10^-5	3.617*10^-5	5.535*10^-5
75.0	1.885*10^-5	3.617*10^-5	5.503*10^-5
80.0	1.854*10^-5	3.617*10^-5	5.472*10^-5
85.0	1.824*10^-5	3.617*10^-5	5.442*10^-5
90.0	1.795*10^-5	3.617*10^-5	5.413*10^-5
95.0	1.767*10^-5	3.617*10^-5	5.385*10^-5
100.0	1.740*10^-5	3.617*10^-5	5.358*10^-5

Table 8E Θ_{min} = 25.0 deg , Θ_{max} = 90.00 deg

	Θ_{min} = 25.0 deg	**INTEGRALS**	Θ_{max} = 90.0 deg
Δ (km)	$I_{earth}(\Theta<\Theta_{min},\Delta)$	$I_{struc}(\Theta_{min},\Theta_{max})$	$I_{earth}+I_{struc}$,
-20.0	3.913*10^-5	2.791*10^-5	6.704*10^-5
-15.0	3.833*10^-5	2.791*10^-5	6.624*10^-5
-10.0	3.733*10^-5	2.791*10^-5	6.524*10^-5
-5.0	3.591*10^-5	2.791*10^-5	6.382*10^-5
.0	3.441*10^-5	2.791*10^-5	6.232*10^-5
5.0	3.099*10^-5	2.791*10^-5	5.889*10^-5
10.0	2.962*10^-5	2.791*10^-5	5.753*10^-5
15.0	2.863*10^-5	2.791*10^-5	5.654*10^-5
20.0	2.784*10^-5	2.791*10^-5	5.575*10^-5
25.0	2.716*10^-5	2.791*10^-5	5.507*10^-5
30.0	2.656*10^-5	2.791*10^-5	5.447*10^-5
35.0	2.602*10^-5	2.791*10^-5	5.393*10^-5
40.0	2.553*10^-5	2.791*10^-5	5.344*10^-5
45.0	2.509*10^-5	2.791*10^-5	5.299*10^-5
50.0	2.466*10^-5	2.791*10^-5	5.257*10^-5
55.0	2.425*10^-5	2.791*10^-5	5.216*10^-5
60.0	2.387*10^-5	2.791*10^-5	5.178*10^-5
65.0	2.350*10^-5	2.791*10^-5	5.141*10^-5
70.0	2.316*10^-5	2.791*10^-5	5.106*10^-5
75.0	2.282*10^-5	2.791*10^-5	5.073*10^-5
80.0	2.250*10^-5	2.791*10^-5	5.041*10^-5
85.0	2.219*10^-5	2.791*10^-5	5.010*10^-5
90.0	2.189*10^-5	2.791*10^-5	4.980*10^-5
95.0	2.160*10^-5	2.791*10^-5	4.951*10^-5
100.0	2.131*10^-5	2.791*10^-5	4.922*10^-5

Table 8F Θ_{min} = 30.0 deg , Θ_{max} = 90.00 deg

	Θ_{min} = 30.0 deg	**INTEGRALS**	Θ_{max} = 90.0 deg
Δ (km)	$I_{earth}(\Theta<\Theta_{min},\Delta)$	$I_{struc}(\Theta_{min},\Theta_{max})$	$I_{earth}+I_{struc}$,
-20.0	4.256*10^-5	2.113*10^-5	6.369*10^-5
-15.0	4.174*10^-5	2.113*10^-5	6.288*10^-5
-10.0	4.074*10^-5	2.113*10^-5	6.187*10^-5
-5.0	3.931*10^-5	2.113*10^-5	6.044*10^-5
.0	3.781*10^-5	2.113*10^-5	5.894*10^-5
5.0	3.437*10^-5	2.113*10^-5	5.550*10^-5
10.0	3.300*10^-5	2.113*10^-5	5.413*10^-5
15.0	3.200*10^-5	2.113*10^-5	5.314*10^-5
20.0	3.120*10^-5	2.113*10^-5	5.233*10^-5
25.0	3.052*10^-5	2.113*10^-5	5.165*10^-5
30.0	2.991*10^-5	2.113*10^-5	5.104*10^-5
35.0	2.937*10^-5	2.113*10^-5	5.050*10^-5
40.0	2.886*10^-5	2.113*10^-5	4.999*10^-5
45.0	2.840*10^-5	2.113*10^-5	4.953*10^-5
50.0	2.796*10^-5	2.113*10^-5	4.909*10^-5
55.0	2.755*10^-5	2.113*10^-5	4.868*10^-5
60.0	2.716*10^-5	2.113*10^-5	4.829*10^-5
65.0	2.679*10^-5	2.113*10^-5	4.792*10^-5
70.0	2.643*10^-5	2.113*10^-5	4.756*10^-5
75.0	2.609*10^-5	2.113*10^-5	4.722*10^-5
80.0	2.576*10^-5	2.113*10^-5	4.689*10^-5
85.0	2.544*10^-5	2.113*10^-5	4.657*10^-5
90.0	2.513*10^-5	2.113*10^-5	4.626*10^-5

95.0	2.483*10^-5	2.113*10^-5	4.596*10^-5
100.0	2.454*10^-5	2.113*10^-5	4.567*10^-5

Table 8G Θ_{min} = 35.0 deg , Θ_{max} = 90.00 deg

	Θ_{min} = 35.0 deg	**INTEGRALS**	Θ_{max} = 90.0 deg
Δ (km)	$I_{earth}(\Theta<\Theta_{min},\Delta)$	$I_{struc}(\Theta_{min},\Theta_{max})$	$I_{earth}+I_{struc}$,
-20.0	4.529*10^-5	1.572*10^-5	6.100*10^-5
-15.0	4.447*10^-5	1.572*10^-5	6.019*10^-5
-10.0	4.346*10^-5	1.572*10^-5	5.917*10^-5
-5.0	4.203*10^-5	1.572*10^-5	5.774*10^-5
.0	4.052*10^-5	1.572*10^-5	5.623*10^-5
5.0	3.708*10^-5	1.572*10^-5	5.279*10^-5
10.0	3.570*10^-5	1.572*10^-5	5.141*10^-5
15.0	3.470*10^-5	1.572*10^-5	5.042*10^-5
20.0	3.389*10^-5	1.572*10^-5	4.961*10^-5
25.0	3.320*10^-5	1.572*10^-5	4.892*10^-5
30.0	3.259*10^-5	1.572*10^-5	4.831*10^-5
35.0	3.204*10^-5	1.572*10^-5	4.776*10^-5
40.0	3.153*10^-5	1.572*10^-5	4.725*10^-5
45.0	3.106*10^-5	1.572*10^-5	4.678*10^-5
50.0	3.062*10^-5	1.572*10^-5	4.634*10^-5
55.0	3.020*10^-5	1.572*10^-5	4.592*10^-5
60.0	2.981*10^-5	1.572*10^-5	4.552*10^-5
65.0	2.943*10^-5	1.572*10^-5	4.515*10^-5
70.0	2.907*10^-5	1.572*10^-5	4.479*10^-5
75.0	2.872*10^-5	1.572*10^-5	4.444*10^-5
80.0	2.839*10^-5	1.572*10^-5	4.410*10^-5
85.0	2.806*10^-5	1.572*10^-5	4.378*10^-5
90.0	2.775*10^-5	1.572*10^-5	4.347*10^-5
95.0	2.745*10^-5	1.572*10^-5	4.316*10^-5
100.0	2.715*10^-5	1.572*10^-5	4.287*10^-5

Table 8H Θ_{min} = 40.0 deg , Θ_{max} = 90.00 deg

	Θ_{min} = 40.0 deg	**INTEGRALS**	Θ_{max} = 90.0 deg
Δ (km)	$I_{earth}(\Theta<\Theta_{min},\Delta)$	$I_{struc}(\Theta_{min},\Theta_{max})$	$I_{earth}+I_{struc}$,
-20.0	4.742*10^-5	1.148*10^-5	5.890*10^-5
-15.0	4.660*10^-5	1.148*10^-5	5.808*10^-5
-10.0	4.559*10^-5	1.148*10^-5	5.706*10^-5
-5.0	4.415*10^-5	1.148*10^-5	5.563*10^-5
.0	4.264*10^-5	1.148*10^-5	5.412*10^-5
5.0	3.920*10^-5	1.148*10^-5	5.067*10^-5
10.0	3.781*10^-5	1.148*10^-5	4.929*10^-5
15.0	3.681*10^-5	1.148*10^-5	4.829*10^-5
20.0	3.600*10^-5	1.148*10^-5	4.748*10^-5
25.0	3.531*10^-5	1.148*10^-5	4.679*10^-5
30.0	3.469*10^-5	1.148*10^-5	4.617*10^-5
35.0	3.414*10^-5	1.148*10^-5	4.562*10^-5
40.0	3.363*10^-5	1.148*10^-5	4.511*10^-5
45.0	3.315*10^-5	1.148*10^-5	4.463*10^-5
50.0	3.271*10^-5	1.148*10^-5	4.419*10^-5
55.0	3.229*10^-5	1.148*10^-5	4.377*10^-5
60.0	3.189*10^-5	1.148*10^-5	4.337*10^-5
65.0	3.151*10^-5	1.148*10^-5	4.299*10^-5
70.0	3.114*10^-5	1.148*10^-5	4.262*10^-5
75.0	3.079*10^-5	1.148*10^-5	4.227*10^-5
80.0	3.045*10^-5	1.148*10^-5	4.193*10^-5
85.0	3.013*10^-5	1.148*10^-5	4.161*10^-5
90.0	2.981*10^-5	1.148*10^-5	4.129*10^-5
95.0	2.950*10^-5	1.148*10^-5	4.098*10^-5
100.0	2.920*10^-5	1.148*10^-5	4.068*10^-5

Table 8I Θ_{min} = 45.0 deg , Θ_{max} = 90.00 deg

	Θ_{min} = 45.0 deg	**INTEGRALS**	Θ_{max} = 90.0 deg
Δ (km)	$I_{earth}(\Theta<\Theta_{min},\Delta)$	$I_{struc}(\Theta_{min},\Theta_{max})$	$I_{earth}+I_{struc}$,
-20.0	4.906*10^-5	8.220*10^-6	5.728*10^-5
-15.0	4.824*10^-5	8.220*10^-6	5.646*10^-5
-10.0	4.722*10^-5	8.220*10^-6	5.544*10^-5
-5.0	4.579*10^-5	8.220*10^-6	5.401*10^-5
.0	4.427*10^-5	8.220*10^-6	5.249*10^-5
5.0	4.083*10^-5	8.220*10^-6	4.904*10^-5
10.0	3.944*10^-5	8.220*10^-6	4.766*10^-5
15.0	3.844*10^-5	8.220*10^-6	4.666*10^-5
20.0	3.762*10^-5	8.220*10^-6	4.584*10^-5
25.0	3.693*10^-5	8.220*10^-6	4.515*10^-5
30.0	3.631*10^-5	8.220*10^-6	4.453*10^-5
35.0	3.575*10^-5	8.220*10^-6	4.397*10^-5
40.0	3.524*10^-5	8.220*10^-6	4.346*10^-5
45.0	3.476*10^-5	8.220*10^-6	4.298*10^-5
50.0	3.432*10^-5	8.220*10^-6	4.254*10^-5
55.0	3.389*10^-5	8.220*10^-6	4.211*10^-5
60.0	3.349*10^-5	8.220*10^-6	4.171*10^-5
65.0	3.311*10^-5	8.220*10^-6	4.133*10^-5
70.0	3.274*10^-5	8.220*10^-6	4.096*10^-5
75.0	3.239*10^-5	8.220*10^-6	4.061*10^-5
80.0	3.205*10^-5	8.220*10^-6	4.027*10^-5
85.0	3.172*10^-5	8.220*10^-6	3.994*10^-5
90.0	3.140*10^-5	8.220*10^-6	3.962*10^-5
95.0	3.109*10^-5	8.220*10^-6	3.931*10^-5
100.0	3.079*10^-5	8.220*10^-6	3.901*10^-5

Tables 9A-9F Surface scatter fractions

Table 9A Θ_{min} = 5.0 deg , Θ_{max} = 32.00 deg

	Θ_{min} = 5.0 deg	**INTEGRALS**	Θ_{max} = 32.0 deg
Δ (km)	$I_{earth}(\Theta<\Theta_{min},\Delta)$	$I_{struc}(\Theta_{min},\Theta_{max})$	$I_{earth}+I_{struc}$,
-20.0	1.788*10^-5	5.072*10^-5	6.860*10^-5
-15.0	1.718*10^-5	5.072*10^-5	6.790*10^-5
-10.0	1.629*10^-5	5.072*10^-5	6.701*10^-5
-5.0	1.498*10^-5	5.072*10^-5	6.570*10^-5
.0	1.360*10^-5	5.072*10^-5	6.431*10^-5
5.0	1.028*10^-5	5.072*10^-5	6.100*10^-5
10.0	9.019*10^-6	5.072*10^-5	5.974*10^-5
15.0	8.145*10^-6	5.072*10^-5	5.886*10^-5
20.0	7.461*10^-6	5.072*10^-5	5.818*10^-5
25.0	6.892*10^-6	5.072*10^-5	5.761*10^-5
30.0	6.404*10^-6	5.072*10^-5	5.712*10^-5
35.0	5.974*10^-6	5.072*10^-5	5.669*10^-5
40.0	5.589*10^-6	5.072*10^-5	5.631*10^-5
45.0	5.240*10^-6	5.072*10^-5	5.596*10^-5
50.0	4.921*10^-6	5.072*10^-5	5.564*10^-5
55.0	4.626*10^-6	5.072*10^-5	5.535*10^-5
60.0	4.353*10^-6	5.072*10^-5	5.507*10^-5
65.0	4.099*10^-6	5.072*10^-5	5.482*10^-5
70.0	3.860*10^-6	5.072*10^-5	5.458*10^-5
75.0	3.636*10^-6	5.072*10^-5	5.435*10^-5
80.0	3.425*10^-6	5.072*10^-5	5.414*10^-5
85.0	3.225*10^-6	5.072*10^-5	5.394*10^-5
90.0	3.036*10^-6	5.072*10^-5	5.375*10^-5
95.0	2.856*10^-6	5.072*10^-5	5.357*10^-5
100.0	2.685*10^-6	5.072*10^-5	5.340*10^-5

Table 9B Θ_{min} = 10.0 deg , Θ_{max} = 32.00 deg

	Θ_{min} = 10.0 deg	**INTEGRALS**	Θ_{max} = 32.0 deg
Δ (km)	$I_{earth}(\Theta<\Theta_{min},\Delta)$	$I_{struc}(\Theta_{min},\Theta_{max})$	$I_{earth}+I_{struc}$,
-20.0	2.433*10^-5	3.825*10^-5	6.258*10^-5
-15.0	2.359*10^-5	3.825*10^-5	6.183*10^-5
-10.0	2.264*10^-5	3.825*10^-5	6.089*10^-5
-5.0	2.128*10^-5	3.825*10^-5	5.953*10^-5
.0	1.984*10^-5	3.825*10^-5	5.809*10^-5
5.0	1.647*10^-5	3.825*10^-5	5.472*10^-5
10.0	1.515*10^-5	3.825*10^-5	5.340*10^-5
15.0	1.423*10^-5	3.825*10^-5	5.248*10^-5
20.0	1.349*10^-5	3.825*10^-5	5.174*10^-5
25.0	1.287*10^-5	3.825*10^-5	5.112*10^-5
30.0	1.233*10^-5	3.825*10^-5	5.057*10^-5
35.0	1.184*10^-5	3.825*10^-5	5.009*10^-5
40.0	1.140*10^-5	3.825*10^-5	4.965*10^-5
45.0	1.100*10^-5	3.825*10^-5	4.925*10^-5
50.0	1.063*10^-5	3.825*10^-5	4.888*10^-5
55.0	1.028*10^-5	3.825*10^-5	4.853*10^-5
60.0	9.953*10^-6	3.825*10^-5	4.820*10^-5
65.0	9.644*10^-6	3.825*10^-5	4.789*10^-5
70.0	9.352*10^-6	3.825*10^-5	4.760*10^-5
75.0	9.073*10^-6	3.825*10^-5	4.732*10^-5
80.0	8.808*10^-6	3.825*10^-5	4.706*10^-5
85.0	8.553*10^-6	3.825*10^-5	4.680*10^-5
90.0	8.309*10^-6	3.825*10^-5	4.656*10^-5
95.0	8.074*10^-6	3.825*10^-5	4.632*10^-5
100.0	7.848*10^-6	3.825*10^-5	4.610*10^-5

Table 9C Θ_{min} = 15.0 deg , Θ_{max} = 90.00 deg

	Θ_{min} = 15.0 deg	**INTEGRALS**	Θ_{max} = 90.0 deg
Δ (km)	$I_{earth}(\Theta<\Theta_{min},\Delta)$	$I_{struc}(\Theta_{min},\Theta_{max})$	$I_{earth}+I_{struc}$,
-20.0	3.001*10^-5	2.713*10^-5	5.714*10^-5
-15.0	2.923*10^-5	2.713*10^-5	5.636*10^-5
-10.0	2.826*10^-5	2.713*10^-5	5.539*10^-5
-5.0	2.687*10^-5	2.713*10^-5	5.400*10^-5
.0	2.540*10^-5	2.713*10^-5	5.253*10^-5
5.0	2.201*10^-5	2.713*10^-5	4.913*10^-5
10.0	2.066*10^-5	2.713*10^-5	4.779*10^-5
15.0	1.971*10^-5	2.713*10^-5	4.684*10^-5
20.0	1.894*10^-5	2.713*10^-5	4.607*10^-5
25.0	1.830*10^-5	2.713*10^-5	4.542*10^-5
30.0	1.773*10^-5	2.713*10^-5	4.485*10^-5
35.0	1.722*10^-5	2.713*10^-5	4.434*10^-5
40.0	1.675*10^-5	2.713*10^-5	4.388*10^-5
45.0	1.632*10^-5	2.713*10^-5	4.345*10^-5
50.0	1.592*10^-5	2.713*10^-5	4.305*10^-5
55.0	1.554*10^-5	2.713*10^-5	4.267*10^-5
60.0	1.519*10^-5	2.713*10^-5	4.232*10^-5
65.0	1.485*10^-5	2.713*10^-5	4.198*10^-5
70.0	1.453*10^-5	2.713*10^-5	4.166*10^-5
75.0	1.423*10^-5	2.713*10^-5	4.135*10^-5
80.0	1.393*10^-5	2.713*10^-5	4.106*10^-5
85.0	1.365*10^-5	2.713*10^-5	4.078*10^-5
90.0	1.338*10^-5	2.713*10^-5	4.050*10^-5
95.0	1.311*10^-5	2.713*10^-5	4.024*10^-5
100.0	1.286*10^-5	2.713*10^-5	3.999*10^-5

Table 9D Θ_{min} = 20.0 deg , Θ_{max} = 32.00 deg

	Θ_{min} = 20.0 deg	**INTEGRALS**	Θ_{max} = 32.0 deg
Δ (km)	$I_{earth}(\Theta<\Theta_{min},\Delta)$	$I_{struc}(\Theta_{min},\Theta_{max})$	$I_{earth}+I_{struc}$,
-20.0	3.496*10^-5	1.736*10^-5	5.233*10^-5
-15.0	3.417*10^-5	1.736*10^-5	5.154*10^-5
-10.0	3.318*10^-5	1.736*10^-5	5.055*10^-5
-5.0	3.178*10^-5	1.736*10^-5	4.914*10^-5
.0	3.029*10^-5	1.736*10^-5	4.765*10^-5
5.0	2.688*10^-5	1.736*10^-5	4.424*10^-5
10.0	2.552*10^-5	1.736*10^-5	4.288*10^-5
15.0	2.455*10^-5	1.736*10^-5	4.191*10^-5
20.0	2.376*10^-5	1.736*10^-5	4.113*10^-5
25.0	2.310*10^-5	1.736*10^-5	4.046*10^-5
30.0	2.251*10^-5	1.736*10^-5	3.987*10^-5
35.0	2.198*10^-5	1.736*10^-5	3.934*10^-5
40.0	2.150*10^-5	1.736*10^-5	3.886*10^-5
45.0	2.105*10^-5	1.736*10^-5	3.841*10^-5
50.0	2.063*10^-5	1.736*10^-5	3.800*10^-5
55.0	2.024*10^-5	1.736*10^-5	3.760*10^-5
60.0	1.987*10^-5	1.736*10^-5	3.723*10^-5
65.0	1.952*10^-5	1.736*10^-5	3.688*10^-5
70.0	1.918*10^-5	1.736*10^-5	3.654*10^-5
75.0	1.885*10^-5	1.736*10^-5	3.622*10^-5
80.0	1.854*10^-5	1.736*10^-5	3.591*10^-5
85.0	1.824*10^-5	1.736*10^-5	3.561*10^-5
90.0	1.795*10^-5	1.736*10^-5	3.532*10^-5
95.0	1.767*10^-5	1.736*10^-5	3.504*10^-5
100.0	1.740*10^-5	1.736*10^-5	3.477*10^-5

Table 9E Θ_{min} = 25.0 deg , Θ_{max} = 32.00 deg

	Θ_{min} = 25.0 deg	**INTEGRALS**	Θ_{max} = 32.0 deg
Δ (km)	$I_{earth}(\Theta<\Theta_{min},\Delta)$	$I_{struc}(\Theta_{min},\Theta_{max})$	$I_{earth}+I_{struc}$
-20.0	3.913*10^-5	9.098*10^-6	4.823*10^-5
-15.0	3.833*10^-5	9.098*10^-6	4.743*10^-5
-10.0	3.733*10^-5	9.098*10^-6	4.642*10^-5
-5.0	3.591*10^-5	9.098*10^-6	4.501*10^-5
.0	3.441*10^-5	9.098*10^-6	4.351*10^-5
5.0	3.099*10^-5	9.098*10^-6	4.008*10^-5
10.0	2.962*10^-5	9.098*10^-6	3.871*10^-5
15.0	2.863*10^-5	9.098*10^-6	3.773*10^-5
20.0	2.784*10^-5	9.098*10^-6	3.694*10^-5
25.0	2.716*10^-5	9.098*10^-6	3.626*10^-5
30.0	2.656*10^-5	9.098*10^-6	3.566*10^-5
35.0	2.602*10^-5	9.098*10^-6	3.512*10^-5
40.0	2.553*10^-5	9.098*10^-6	3.463*10^-5
45.0	2.509*10^-5	9.098*10^-6	3.418*10^-5
50.0	2.466*10^-5	9.098*10^-6	3.375*10^-5
55.0	2.425*10^-5	9.098*10^-6	3.335*10^-5
60.0	2.387*10^-5	9.098*10^-6	3.297*10^-5
65.0	2.350*10^-5	9.098*10^-6	3.260*10^-5
70.0	2.316*10^-5	9.098*10^-6	3.225*10^-5
75.0	2.282*10^-5	9.098*10^-6	3.192*10^-5
80.0	2.250*10^-5	9.098*10^-6	3.160*10^-5
85.0	2.219*10^-5	9.098*10^-6	3.129*10^-5
90.0	2.189*10^-5	9.098*10^-6	3.099*10^-5
95.0	2.160*10^-5	9.098*10^-6	3.069*10^-5
100.0	2.131*10^-5	9.098*10^-6	3.041*10^-5

Table 9F Θ_{min} = 30.0 deg , Θ_{max} = 32.00 deg

	Θ_{min} = 30.0 deg	**INTEGRALS**	Θ_{max} = 32.0 deg
Δ (km)	$I_{earth}(\Theta<\Theta_{min},\Delta)$	$I_{struc}(\Theta_{min},\Theta_{max})$	$I_{earth}+I_{struc}$,
-20.0	4.256*10^-5	2.320*10^-6	4.488*10^-5
-15.0	4.174*10^-5	2.320*10^-6	4.406*10^-5
-10.0	4.074*10^-5	2.320*10^-6	4.306*10^-5
-5.0	3.931*10^-5	2.320*10^-6	4.163*10^-5
.0	3.781*10^-5	2.320*10^-6	4.013*10^-5
5.0	3.437*10^-5	2.320*10^-6	3.669*10^-5
10.0	3.300*10^-5	2.320*10^-6	3.532*10^-5
15.0	3.200*10^-5	2.320*10^-6	3.432*10^-5
20.0	3.120*10^-5	2.320*10^-6	3.352*10^-5
25.0	3.052*10^-5	2.320*10^-6	3.284*10^-5
30.0	2.991*10^-5	2.320*10^-6	3.223*10^-5
35.0	2.937*10^-5	2.320*10^-6	3.169*10^-5
40.0	2.886*10^-5	2.320*10^-6	3.118*10^-5
45.0	2.840*10^-5	2.320*10^-6	3.072*10^-5
50.0	2.796*10^-5	2.320*10^-6	3.028*10^-5
55.0	2.755*10^-5	2.320*10^-6	2.987*10^-5
60.0	2.716*10^-5	2.320*10^-6	2.948*10^-5
65.0	2.679*10^-5	2.320*10^-6	2.911*10^-5
70.0	2.643*10^-5	2.320*10^-6	2.875*10^-5
75.0	2.609*10^-5	2.320*10^-6	2.841*10^-5
80.0	2.576*10^-5	2.320*10^-6	2.808*10^-5
85.0	2.544*10^-5	2.320*10^-6	2.776*10^-5
90.0	2.513*10^-5	2.320*10^-6	2.745*10^-5
95.0	2.483*10^-5	2.320*10^-6	2.715*10^-5
100.0	2.454*10^-5	2.320*10^-6	2.686*10^-5

95.0	8.702*10^-5	5.241*10^-5	1.394*10^-4
100.0	8.115*10^-5	5.241*10^-5	1.336*10^-4

Table 11 Diffractive scatter estimates

Table 11A Θ_{min} = 5.0 deg , Θ_{max} = 90.00 deg

	Θ_{min} = 5.0 deg	**INTEGRALS**	Θ_{max} = 90.0 deg
Δ (km)	$I_{earth}(\Theta<\Theta_{min},\Delta)$	$I_{struc}(\Theta_{min},\Theta_{max})$	$I_{earth}+I_{struc}$,
-20.0	2.134*10^-2	1.104*10^-4	2.145*10^-2
-15.0	2.134*10^-2	1.104*10^-4	2.145*10^-2
-10.0	2.130*10^-2	1.104*10^-4	2.141*10^-2
-5.0	2.105*10^-2	1.104*10^-4	2.116*10^-2
.0	1.686*10^-2	1.104*10^-4	1.697*10^-2
5.0	1.962*10^-3	1.104*10^-4	2.072*10^-3
10.0	1.025*10^-3	1.104*10^-4	1.136*10^-3
15.0	6.713*10^-4	1.104*10^-4	7.816*10^-4
20.0	4.879*10^-4	1.104*10^-4	5.983*10^-4
25.0	3.814*10^-4	1.104*10^-4	4.918*10^-4
30.0	3.084*10^-4	1.104*10^-4	4.188*10^-4
35.0	2.552*10^-4	1.104*10^-4	3.655*10^-4
40.0	2.165*10^-4	1.104*10^-4	3.268*10^-4
45.0	1.860*10^-4	1.104*10^-4	2.964*10^-4
50.0	1.612*10^-4	1.104*10^-4	2.716*10^-4
55.0	1.415*10^-4	1.104*10^-4	2.519*10^-4
60.0	1.250*10^-4	1.104*10^-4	2.354*10^-4
65.0	1.109*10^-4	1.104*10^-4	2.213*10^-4
70.0	9.902*10^-5	1.104*10^-4	2.094*10^-4
75.0	8.884*10^-5	1.104*10^-4	1.992*10^-4
80.0	7.979*10^-5	1.104*10^-4	1.902*10^-4
85.0	7.193*10^-5	1.104*10^-4	1.823*10^-4
90.0	6.507*10^-5	1.104*10^-4	1.754*10^-4
95.0	5.888*10^-5	1.104*10^-4	1.693*10^-4
100.0	5.333*10^-5	1.104*10^-4	1.637*10^-4

Table 11B Θ_{min} = 10.0 deg , Θ_{max} = 90.00 deg

	Θ_{min} = 10.0 deg	**INTEGRALS**	Θ_{max} = 90.0 deg
Δ (km)	$I_{earth}(\Theta<\Theta_{min},\Delta)$	$I_{struc}(\Theta_{min},\Theta_{max})$	$I_{earth}+I_{struc}$,
-20.0	2.141*10^-2	5.241*10^-5	2.146*10^-2
-15.0	2.140*10^-2	5.241*10^-5	2.146*10^-2
-10.0	2.137*10^-2	5.241*10^-5	2.142*10^-2
-5.0	2.112*10^-2	5.241*10^-5	2.117*10^-2
.0	1.690*10^-2	5.241*10^-5	1.695*10^-2
5.0	1.996*10^-3	5.241*10^-5	2.048*10^-3
10.0	1.059*10^-3	5.241*10^-5	1.111*10^-3
15.0	7.045*10^-4	5.241*10^-5	7.569*10^-4
20.0	5.209*10^-4	5.241*10^-5	5.733*10^-4
25.0	4.140*10^-4	5.241*10^-5	4.664*10^-4
30.0	3.407*10^-4	5.241*10^-5	3.931*10^-4
35.0	2.872*10^-4	5.241*10^-5	3.396*10^-4
40.0	2.481*10^-4	5.241*10^-5	3.005*10^-4
45.0	2.174*10^-4	5.241*10^-5	2.698*10^-4
50.0	1.923*10^-4	5.241*10^-5	2.447*10^-4
55.0	1.722*10^-4	5.241*10^-5	2.246*10^-4
60.0	1.554*10^-4	5.241*10^-5	2.079*10^-4
65.0	1.410*10^-4	5.241*10^-5	1.934*10^-4
70.0	1.288*10^-4	5.241*10^-5	1.812*10^-4
75.0	1.183*10^-4	5.241*10^-5	1.707*10^-4
80.0	1.089*10^-4	5.241*10^-5	1.613*10^-4
85.0	1.007*10^-4	5.241*10^-5	1.531*10^-4
90.0	9.354*10^-5	5.241*10^-5	1.459*10^-4

Table 11C Θ_{min} = 15.0 deg , Θ_{max} = 90.00 deg

	Θ_{min} = 15.0 deg	**INTEGRALS**	Θ_{max} = 90.0 deg
Δ (km)	$I_{earth}(\Theta<\Theta_{min},\Delta)$	$I_{struc}(\Theta_{min},\Theta_{max})$	$I_{earth}+I_{struc}$,
-20.0	2.143*10^-2	3.588*10^-5	2.147*10^-2
-15.0	2.143*10^-2	3.588*10^-5	2.146*10^-2
-10.0	2.139*10^-2	3.588*10^-5	2.143*10^-2
-5.0	2.114*10^-2	3.588*10^-5	2.118*10^-2
.0	1.691*10^-2	3.588*10^-5	1.694*10^-2
5.0	2.007*10^-3	3.588*10^-5	2.043*10^-3
10.0	1.070*10^-3	3.588*10^-5	1.106*10^-3
15.0	7.157*10^-4	3.588*10^-5	7.515*10^-4
20.0	5.320*10^-4	3.588*10^-5	5.678*10^-4
25.0	4.250*10^-4	3.588*10^-5	4.609*10^-4
30.0	3.517*10^-4	3.588*10^-5	3.876*10^-4
35.0	2.981*10^-4	3.588*10^-5	3.340*10^-4
40.0	2.590*10^-4	3.588*10^-5	2.949*10^-4
45.0	2.282*10^-4	3.588*10^-5	2.641*10^-4
50.0	2.030*10^-4	3.588*10^-5	2.389*10^-4
55.0	1.829*10^-4	3.588*10^-5	2.188*10^-4
60.0	1.661*10^-4	3.588*10^-5	2.020*10^-4
65.0	1.515*10^-4	3.588*10^-5	1.874*10^-4
70.0	1.393*10^-4	3.588*10^-5	1.752*10^-4
75.0	1.287*10^-4	3.588*10^-5	1.646*10^-4
80.0	1.193*10^-4	3.588*10^-5	1.552*10^-4
85.0	1.111*10^-4	3.588*10^-5	1.469*10^-4
90.0	1.038*10^-4	3.588*10^-5	1.397*10^-4
95.0	9.726*10^-5	3.588*10^-5	1.331*10^-4
100.0	9.132*10^-5	3.588*10^-5	1.272*10^-4

Table 11D Θ_{min} = 20.0 deg , Θ_{max} = 90.00 deg

	Θ_{min} = 20.0 deg	**INTEGRALS**	Θ_{max} = 90.0 deg
Δ (km)	$I_{earth}(\Theta<\Theta_{min},\Delta)$	$I_{struc}(\Theta_{min},\Theta_{max})$	$I_{earth}+I_{struc}$,
-20.0	2.144*10^-2	2.079*10^-5	2.146*10^-2
-15.0	2.144*10^-2	2.079*10^-5	2.146*10^-2
-10.0	2.140*10^-2	2.079*10^-5	2.142*10^-2
-5.0	2.115*10^-2	2.079*10^-5	2.117*10^-2
.0	1.691*10^-2	2.079*10^-5	1.693*10^-2
5.0	2.013*10^-3	2.079*10^-5	2.033*10^-3
10.0	1.076*10^-3	2.079*10^-5	1.096*10^-3
15.0	7.212*10^-4	2.079*10^-5	7.420*10^-4
20.0	5.375*10^-4	2.079*10^-5	5.583*10^-4
25.0	4.305*10^-4	2.079*10^-5	4.513*10^-4
30.0	3.572*10^-4	2.079*10^-5	3.780*10^-4
35.0	3.035*10^-4	2.079*10^-5	3.243*10^-4
40.0	2.644*10^-4	2.079*10^-5	2.852*10^-4
45.0	2.336*10^-4	2.079*10^-5	2.544*10^-4
50.0	2.084*10^-4	2.079*10^-5	2.292*10^-4
55.0	1.883*10^-4	2.079*10^-5	2.091*10^-4
60.0	1.715*10^-4	2.079*10^-5	1.922*10^-4
65.0	1.569*10^-4	2.079*10^-5	1.777*10^-4
70.0	1.446*10^-4	2.079*10^-5	1.654*10^-4
75.0	1.341*10^-4	2.079*10^-5	1.548*10^-4
80.0	1.246*10^-4	2.079*10^-5	1.454*10^-4
85.0	1.163*10^-4	2.079*10^-5	1.371*10^-4
90.0	1.091*10^-4	2.079*10^-5	1.299*10^-4
95.0	1.025*10^-4	2.079*10^-5	1.233*10^-4
100.0	9.653*10^-5	2.079*10^-5	1.173*10^-4

Table 11E Θ_{min} = 25.0 deg , Θ_{max} = 90.00 deg

	Θ_{min} = 25.0 deg	**INTEGRALS**	Θ_{max} = 90.0 deg
Δ (km)	$I_{earth}(\Theta<\Theta_{min},\Delta)$	$I_{struc}(\Theta_{min},\Theta_{max})$	$I_{earth}+I_{struc}$,
-20.0	2.145*10^-2	1.704*10^-5	2.147*10^-2
-15.0	2.145*10^-2	1.704*10^-5	2.146*10^-2
-10.0	2.141*10^-2	1.704*10^-5	2.143*10^-2
-5.0	2.116*10^-2	1.704*10^-5	2.118*10^-2
.0	1.692*10^-2	1.704*10^-5	1.693*10^-2
5.0	2.016*10^-3	1.704*10^-5	2.033*10^-3
10.0	1.079*10^-3	1.704*10^-5	1.096*10^-3
15.0	7.245*10^-4	1.704*10^-5	7.415*10^-4
20.0	5.408*10^-4	1.704*10^-5	5.578*10^-4
25.0	4.338*10^-4	1.704*10^-5	4.509*10^-4
30.0	3.604*10^-4	1.704*10^-5	3.775*10^-4
35.0	3.068*10^-4	1.704*10^-5	3.238*10^-4
40.0	2.677*10^-4	1.704*10^-5	2.847*10^-4
45.0	2.369*10^-4	1.704*10^-5	2.539*10^-4
50.0	2.117*10^-4	1.704*10^-5	2.287*10^-4
55.0	1.915*10^-4	1.704*10^-5	2.086*10^-4
60.0	1.747*10^-4	1.704*10^-5	1.917*10^-4
65.0	1.601*10^-4	1.704*10^-5	1.772*10^-4
70.0	1.478*10^-4	1.704*10^-5	1.649*10^-4
75.0	1.373*10^-4	1.704*10^-5	1.543*10^-4
80.0	1.278*10^-4	1.704*10^-5	1.448*10^-4
85.0	1.195*10^-4	1.704*10^-5	1.366*10^-4
90.0	1.123*10^-4	1.704*10^-5	1.293*10^-4
95.0	1.057*10^-4	1.704*10^-5	1.227*10^-4
100.0	9.968*10^-5	1.704*10^-5	1.167*10^-4

Table 11F Θ_{min} = 30.0 deg , Θ_{max} = 90.00 deg

	Θ_{min} = 30.0 deg	**INTEGRALS**	Θ_{max} = 90.0 deg
Δ (km)	$I_{earth}(\Theta<\Theta_{min},\Delta)$	$I_{struc}(\Theta_{min},\Theta_{max})$	$I_{earth}+I_{struc}$,
-20.0	2.145*10^-2	1.250*10^-5	2.147*10^-2
-15.0	2.145*10^-2	1.250*10^-5	2.146*10^-2
-10.0	2.141*10^-2	1.250*10^-5	2.143*10^-2
-5.0	2.116*10^-2	1.250*10^-5	2.118*10^-2
.0	1.692*10^-2	1.250*10^-5	1.693*10^-2
5.0	2.018*10^-3	1.250*10^-5	2.031*10^-3
10.0	1.081*10^-3	1.250*10^-5	1.094*10^-3
15.0	7.267*10^-4	1.250*10^-5	7.392*10^-4
20.0	5.429*10^-4	1.250*10^-5	5.554*10^-4
25.0	4.360*10^-4	1.250*10^-5	4.485*10^-4
30.0	3.626*10^-4	1.250*10^-5	3.751*10^-4
35.0	3.090*10^-4	1.250*10^-5	3.215*10^-4
40.0	2.698*10^-4	1.250*10^-5	2.823*10^-4
45.0	2.390*10^-4	1.250*10^-5	2.515*10^-4
50.0	2.138*10^-4	1.250*10^-5	2.263*10^-4
55.0	1.937*10^-4	1.250*10^-5	2.062*10^-4
60.0	1.768*10^-4	1.250*10^-5	1.893*10^-4
65.0	1.623*10^-4	1.250*10^-5	1.748*10^-4
70.0	1.500*10^-4	1.250*10^-5	1.625*10^-4
75.0	1.395*10^-4	1.250*10^-5	1.520*10^-4
80.0	1.300*10^-4	1.250*10^-5	1.425*10^-4
85.0	1.218*10^-4	1.250*10^-5	1.343*10^-4
90.0	1.145*10^-4	1.250*10^-5	1.270*10^-4
95.0	1.079*10^-4	1.250*10^-5	1.204*10^-4

100.0	1.020*10^-4	1.250*10^-5	1.145*10^-4

Table 11G Θ_{min} = 35.0 deg , Θ_{max} = 90.00 deg

	Θ_{min} = 35.0 deg	**INTEGRALS**	Θ_{max} = 90.0 deg
Δ (km)	$I_{earth}(\Theta<\Theta_{min},\Delta)$	$I_{struc}(\Theta_{min},\Theta_{max})$	$I_{earth}+I_{struc}$,
-20.0	2.146*10^-2	8.810*10^-6	2.147*10^-2
-15.0	2.145*10^-2	8.810*10^-6	2.146*10^-2
-10.0	2.142*10^-2	8.810*10^-6	2.143*10^-2
-5.0	2.117*10^-2	8.810*10^-6	2.117*10^-2
.0	1.692*10^-2	8.810*10^-6	1.693*10^-2
5.0	2.020*10^-3	8.810*10^-6	2.028*10^-3
10.0	1.083*10^-3	8.810*10^-6	1.091*10^-3
15.0	7.282*10^-4	8.810*10^-6	7.370*10^-4
20.0	5.444*10^-4	8.810*10^-6	5.532*10^-4
25.0	4.375*10^-4	8.810*10^-6	4.463*10^-4
30.0	3.641*10^-4	8.810*10^-6	3.729*10^-4
35.0	3.105*10^-4	8.810*10^-6	3.193*10^-4
40.0	2.713*10^-4	8.810*10^-6	2.801*10^-4
45.0	2.405*10^-4	8.810*10^-6	2.493*10^-4
50.0	2.153*10^-4	8.810*10^-6	2.241*10^-4
55.0	1.952*10^-4	8.810*10^-6	2.040*10^-4
60.0	1.783*10^-4	8.810*10^-6	1.871*10^-4
65.0	1.638*10^-4	8.810*10^-6	1.726*10^-4
70.0	1.515*10^-4	8.810*10^-6	1.603*10^-4
75.0	1.409*10^-4	8.810*10^-6	1.497*10^-4
80.0	1.315*10^-4	8.810*10^-6	1.403*10^-4
85.0	1.232*10^-4	8.810*10^-6	1.320*10^-4
90.0	1.160*10^-4	8.810*10^-6	1.248*10^-4
95.0	1.094*10^-4	8.810*10^-6	1.182*10^-4
100.0	1.035*10^-4	8.810*10^-6	1.123*10^-4

Table 11H Θ_{min} = 40.0 deg , Θ_{max} = 90.00 deg

	Θ_{min} = 40.0 deg	**INTEGRALS**	Θ_{max} = 90.0 deg
Δ (km)	$I_{earth}(\Theta<\Theta_{min},\Delta)$	$I_{struc}(\Theta_{min},\Theta_{max})$	$I_{earth}+I_{struc}$,
-20.0	2.146*10^-2	6.670*10^-6	2.147*10^-2
-15.0	2.145*10^-2	6.670*10^-6	2.146*10^-2
-10.0	2.142*10^-2	6.670*10^-6	2.143*10^-2
-5.0	2.117*10^-2	6.670*10^-6	2.117*10^-2
.0	1.692*10^-2	6.670*10^-6	1.693*10^-2
5.0	2.021*10^-3	6.670*10^-6	2.027*10^-3
10.0	1.084*10^-3	6.670*10^-6	1.090*10^-3
15.0	7.293*10^-4	6.670*10^-6	7.360*10^-4
20.0	5.455*10^-4	6.670*10^-6	5.522*10^-4
25.0	4.386*10^-4	6.670*10^-6	4.453*10^-4
30.0	3.652*10^-4	6.670*10^-6	3.719*10^-4
35.0	3.116*10^-4	6.670*10^-6	3.182*10^-4
40.0	2.724*10^-4	6.670*10^-6	2.791*10^-4
45.0	2.416*10^-4	6.670*10^-6	2.483*10^-4
50.0	2.164*10^-4	6.670*10^-6	2.231*10^-4
55.0	1.963*10^-4	6.670*10^-6	2.029*10^-4
60.0	1.794*10^-4	6.670*10^-6	1.861*10^-4
65.0	1.649*10^-4	6.670*10^-6	1.715*10^-4
70.0	1.526*10^-4	6.670*10^-6	1.593*10^-4
75.0	1.420*10^-4	6.670*10^-6	1.487*10^-4
80.0	1.326*10^-4	6.670*10^-6	1.393*10^-4
85.0	1.243*10^-4	6.670*10^-6	1.310*10^-4
90.0	1.171*10^-4	6.670*10^-6	1.237*10^-4
95.0	1.105*10^-4	6.670*10^-6	1.172*10^-4
100.0	1.045*10^-4	6.670*10^-6	1.112*10^-4

Table 11I Θ_{min} = 45.0 deg , Θ_{max} = 90.00 deg

	Θ_{min} = 45.0 deg	**INTEGRALS**	Θ_{max} = 90.0 deg
Δ (km)	$I_{earth}(\Theta<\Theta_{min},\Delta)$	$I_{struc}(\Theta_{min},\Theta_{max})$	$I_{earth}+I_{struc}$,
-20.0	2.146*10^-2	4.776*10^-6	2.146*10^-2
-15.0	2.146*10^-2	4.776*10^-6	2.146*10^-2
-10.0	2.142*10^-2	4.776*10^-6	2.143*10^-2
-5.0	2.117*10^-2	4.776*10^-6	2.117*10^-2
.0	1.692*10^-2	4.776*10^-6	1.693*10^-2
5.0	2.021*10^-3	4.776*10^-6	2.026*10^-3
10.0	1.085*10^-3	4.776*10^-6	1.089*10^-3
15.0	7.301*10^-4	4.776*10^-6	7.349*10^-4
20.0	5.464*10^-4	4.776*10^-6	5.511*10^-4
25.0	4.394*10^-4	4.776*10^-6	4.442*10^-4
30.0	3.660*10^-4	4.776*10^-6	3.708*10^-4
35.0	3.124*10^-4	4.776*10^-6	3.172*10^-4
40.0	2.733*10^-4	4.776*10^-6	2.780*10^-4
45.0	2.424*10^-4	4.776*10^-6	2.472*10^-4
50.0	2.172*10^-4	4.776*10^-6	2.220*10^-4
55.0	1.971*10^-4	4.776*10^-6	2.019*10^-4
60.0	1.802*10^-4	4.776*10^-6	1.850*10^-4
65.0	1.657*10^-4	4.776*10^-6	1.704*10^-4
70.0	1.534*10^-4	4.776*10^-6	1.582*10^-4
75.0	1.428*10^-4	4.776*10^-6	1.476*10^-4
80.0	1.334*10^-4	4.776*10^-6	1.382*10^-4
85.0	1.251*10^-4	4.776*10^-6	1.299*10^-4
90.0	1.179*10^-4	4.776*10^-6	1.226*10^-4
95.0	1.113*10^-4	4.776*10^-6	1.161*10^-4
100.0	1.053*10^-4	4.776*10^-6	1.101*10^-4

Appendix B : 21- channel Atmospheric radiance curves, figures B1 - B21

In figures B1-B21, fiducial atmospheric radiance profiles with height are plotted using the logarithmic RH scale. The logarithmic LH scale is shifted up by a factor 100, relative to the RH scale, enabling the same profile to be used as a curve following the 1% level of the radiance curve as well. The NEN and 0.25 NEN levels are drawn for each scale. The LOS height where the 1% curve crosses the 0.25 NEN level in each channel (use the LH scale) is denoted the 'cross-over height' in the text (section 13) above which the 0.25 NEN level becomes the background level driving the design and below which the 1% radiance level is the background driver.

Most of the table 16A, 16B and 16C values, which are diffractive scatter estimates for each HIRDLS channel as a function of LOS height, are plotted using the LH scales of each of the figures B1-B21. . They are plotted using the symbol -⊕- .

Most of the table 17A, 17B and 17C values, which are surface scatter estimates for each HIRDLS channel as a function of LOS height, are plotted using the LH scales of each of the figures B1-B21. They are plotted using the symbol -×- .

The atmospheric radiance curves are taken ,with thanks, from TC-HIR-90, authored and computed by Chris Halvorsen of NCAR.